Department of Physics and Astronomy
Heidelberg University

Bachelor Thesis in Physics
submitted by

Yukai Zhao

born in Kaiserslautern (Germany)

2023

Exploiting the potential of upstream track reconstruction to enhance the sensitivity of CP asymmetry measurements in $D^0 \to K_S^0 K_S^0$ decays in Run 3 at LHCb

This Bachelor Thesis has been carried out by Yukai Zhao at the
Physikalisches Institut in Heidelberg
under the supervision of
Prof. Dr. Stephanie Hansmann-Menzemer

Abstract

The investigation of CP violation in $D^0 \rightarrow K_S^0 K_S^0$ decays is interesting to probe the Standard Model of particle physics and serve for potential beyond Standard Model contributions. However, the current measurement is limited by the available data size. In this study, an approach to increase the statistical power by exploiting upstream tracks for the reconstruction of the decay channel is investigated. The analysis, based on Monte Carlo simulations of Run 3 data, reveals that integrating upstream track reconstruction yields an enhancement of the statistical power of at least 3.1%. Moreover, looking ahead to future Runs, an improvement up to 12.7% might become feasible.

Zusammenfassung

Die Untersuchung der CP Verletzung in $D^0 \rightarrow K_S^0 K_S^0$ Zerfällen ist besonders interessant, um das Standardmodell der Teilchenphysik auf mögliche Beiträge jenseits des Standardmodells zu überprüfen. Die aktuelle Messung wird jedoch durch die verfügbare Datengröße begrenzt. In dieser Arbeit wird ein Ansatz zur Steigerung der Statistik untersucht, indem Upstream Spuren zur Rekonstruktion des Zerfallskanals genutzt werden. Die Analyse, welche sich auf Monte Carlo Simulationen von Run 3 Daten basiert, zeigt, dass die Integration der Upstream Spuren eine Steigerung der statistischen Aussagekraft von mindestens $3,1\%$ ergibt. Darüber hinaus könnte eine Verbesserung von bis zu $12,7\%$ für zukünftige Runs realisierbar sein.

Contents

1 Introduction **1**

2 Theoretical background **2**

2.1 The Standard Model 2

2.2 The $D^0 \to K^0_S K^0_S$ decay channel 3

2.3 Current state of the CP asymmetry measurement in $D^0 \to K^0_S K^0_S$ decays 5

3 The LHCb experiment **6**

3.1 The Large Hadron Collider 6

3.2 The LHCb detector 6

3.2.1 Tracking detectors 7

3.2.2 Particle identification 8

3.2.3 Trigger system 9

3.2.4 Track reconstruction 10

3.3 Monte Carlo simulations 11

4 Overview of the analysis **13**

4.1 Impact on mass resolution using upstream tracks 14

5 Trigger selection **18**

5.1 Background analysis for K^0_S using upstream track 18

5.2 Selection at first stage of high level trigger 19

5.3 Selection at second stage of high level trigger 20

5.3.1 Momentum and transverse momentum cut of the HLT2 trigger line . . 21

5.3.2 Efficiency of the trigger line 22

6 Sensitivity estimation **24**

6.1 Methodology 24

6.2 Results of the sensitivity estimation 25

7 Exploiting upstream tracks for soft pion reconstruction **29**

7.1 Estimate of potential gain in sensitivity 30

8 Conclusion **33**

A Fit results of the K^0_S mass distributions **36**

B Fit results for long track π_{soft} samples **37**

C Fit results for upstream track π_{soft} samples **39**

Bibliography **42**

Chapter 1

Introduction

The Standard Model of particle physics is a theory which describes all known elementary particles and their interactions. While it has successfully predicted and described current experimental data, it falls short in explaining certain phenomena observed in nature such as baryon asymmetry, gravity, and the existence of dark matter. Thus, it is believed that the Standard Model is only a low-energy approximation of a more general theory.

The Standard Model is probed in measurements at the highest energies as well as in precision measurements. The study of particle antiparticle asymmetries in D meson decays is promising in the search for beyond Standard Model phenomena in precision measurements. In addition, the neutral D system is the only one where the up quark is involved. Thus, the decay $D^0 \rightarrow K_S^0 K_S^0$ is especially interesting with an upper limit of 1.1% [1] for the CP asymmetry based on Standard Model predictions. Using Run 2 data from the LHCb experiment a value of $A^{\mathrm{CP}}(D^0 \rightarrow K_S^0 K_S^0) = (-3.1 \pm 1.2 \pm 0.4 \pm 0.2)\%$ [2] has been measured, where the first uncertainty is statistical, the second systematic and the third due to the uncertainty of the asymmetry of the calibration channel. This asymmetry is larger than expected but it is still compatible with the theoretical predictions, given the large statistical and theoretical uncertainties.

The upgraded LHCb detector for Run 3 features a full software trigger which allows the reconstruction of upstream tracks at the earliest stage of the trigger sequence. In this thesis, the impact resulting from these track inclusion on the sensitivity of the CP asymmetry measurement in $D^0 \rightarrow K_S^0 K_S^0$ decays is studied.

Chapter 2

Theoretical background

2.1 The Standard Model

The Standard Model (SM) of particle physics [3] is the most self-consistent Quantum Field Theory (QFT) which describes elementary particles and their interactions. In Figure 2.1, all fundamental particles of the Standard Model are visualized. It consists of 12 elementary particles of spin $1/2$, known as fermions, which can be categorized into three generations. Each generation is composed of two leptons and two quarks. Quarks can be further classified as up-type quarks, carrying an electric charge of $+2/3$, and down-type quarks, carrying an electric charge of $-1/3$. A lepton generation consists of a charged lepton and an associated neutrino. The charged lepton has an electric charge of -1, while the neutrino is charge neutral. These neutrinos are considered massless within the SM. Furthermore, each particle in the SM has an associated antiparticle, which carries the opposite quantum numbers.
The first generation includes the up-quark (u), down-quark (d), electron (e^-), and electron neutrino (ν_e). The second generation consists of the charm-quark (c), strange-quark (s), muon (μ^-), and muon neutrino (ν_μ). Lastly, the third generation is composed of the top-quark (t), bottom-quark (b), tau (τ), and tau neutrino (ν_τ). The second and third generations exhibit the same interactions and properties as the first generation but have larger masses compared to previous generations.
The interactions between elementary particles are described by different Quantum Field Theories. For electromagnetism, the theory is known as Quantum Electrodynamics (QED), where the interaction between charged particles is mediated by the exchange of a photon. In the case of the strong interaction, which occurs exclusively between quarks and leads to their hadronization, the theory is called Quantum Chromodynamics (QCD) and is mediated by gluons. The weak charged-current interaction is mediated by the charged $W^\pm$ bosons, while the weak neutral-current interaction is mediated by the Z boson. These force-carrying particles, known as bosons, have a spin of 1. Furthermore, the photon and gluon are massless particles, while the mediating particles for the weak interaction are approximately eighty times more massive than the proton.
In addition to the elementary particles and force carriers, there is a standalone scalar Higgs

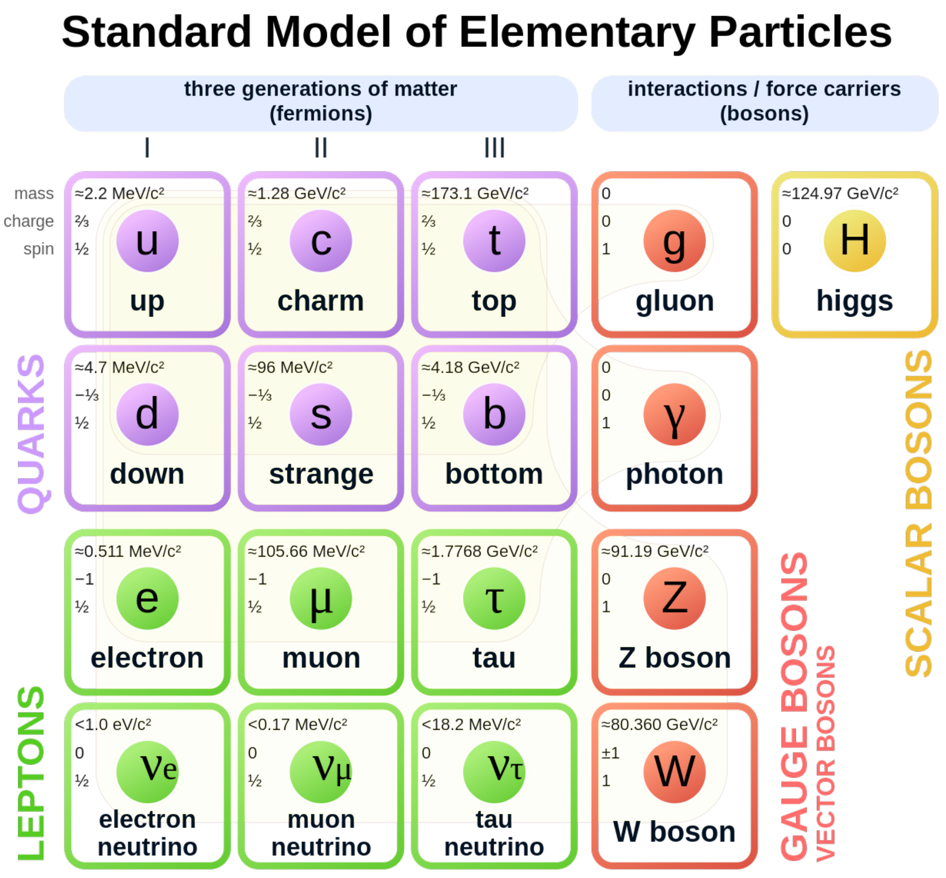

Figure 2.1: The fundamental particles of the Standard Model [4].

boson with spin 0. The Higgs boson plays a crucial role by providing the mechanism through which all other particles acquire their masses.

2.2 The $D^0 \to K_S^0 K_S^0$ decay channel

The charge-parity (CP) asymmetry A^{CP} between states produced as D^0 or $\bar{D}^0$ decaying to the CP eigenstate $K_S^0 K_S^0$ is defined as:

$$A^{\mathrm{CP}} = \frac{\Gamma(D^0 \to K_S^0 K_S^0) - \Gamma(\bar{D}^0 \to K_S^0 K_S^0)}{\Gamma(D^0 \to K_S^0 K_S^0) + \Gamma(\bar{D}^0 \to K_S^0 K_S^0)} \tag{2.2.1}$$

where Γ denotes the rate of the D^0 or $\bar{D}^0$ decay. The contributions of the dominant processes in the $D^0 \to K_S^0 K_S^0$ decay channel can be visualized by the Feynman diagrams shown in Figure 2.2. This decay is single Cabibbo suppressed (SCS) as it involves a single off-diagonal CKM (Cabibbo-Kobayashi-Maskawa) matrix transition.

When a D^0 meson, composed of a charm-quark and an up-antiquark, is produced directly from the proton-proton (pp) collision, it is for this decay mode not possible to differentiate between a D^0 and a $\bar{D}^0$ decay due to the CP symmetric final state. Therefore, a tagging procedure is employed to gain information about the flavour content of the D^0 which is crucial

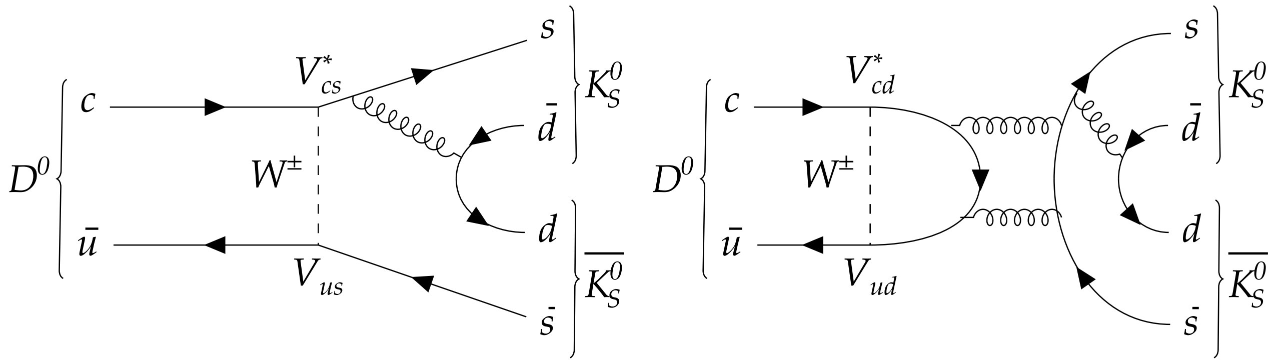

Figure 2.2: Feynman diagrams of the dominant $D^0 \to K^0_S K^0_S$ decay processes.

for the CP asymmetry measurement. This procedure involves the strong decay of $D^{*+} \to D^0\pi^+$ ($D^{*-} \to \bar{D}^0\pi^-$), which conserves CP. Thus, the charge of the pion is used to determine the flavour of the D^0. Since the mass difference between D^{*+} and D^0 is (145.42 ± 0.07) MeV/c^2 [5], slightly greater than the mass of a pion ($m(\pi^+) = (139.57039 \pm 0.00018)$ MeV/c^2 [5]), the pion produced in this decay has low momentum and is hence referred to as a soft pion π_{soft}. The D^{*+} has a short lifetime due to the strong decay. This implies its decay vertex is consistent with the primary vertex of the D^*.
In the majority of the cases, the D^* is produced in the primary pp collision (prompt decays). However, D^* can be also produced in the decay of a b hadron (secondary decays). While the CP asymmetry is the same in the two cases, the production asymmetry is different, and the effect has to be properly taken into account in the analysis.

By making use of this tagging procedure, the CP asymmetry measurement in the $D^0 \to K^0_S K^0_S$ decay channel is affected by both the production asymmetry of the D^* and the detection asymmetry of the π_{soft}. To mitigate these effects, each event is weighted using the $D^0 \to K^+K^-$ calibration channel.
Additionally, the D^* originating from secondary decays are affected by different production asymmetry depending on the b-hadron species. Consequently, secondary decays are typically treated as background, and selection requirements are applied to reduce them. Specifically, they are removed using information on the D^0 vertex displacement with respect to the primary vertex. However, the effectiveness of such selection depends on the D^0 vertex resolution, which degrades when downstream or upstream tracks (Section 3.2.4 for definition) are involved. For this reason, secondary decays are treated as signals by utilizing the same calibration channel to nullify the production asymmetries. For more detailed reading refer to [2].

Furthermore, the $D^0 - \bar{D}^0$ mixing is negligible for the analysis, due to the slow mixing rate. The reconstruction of K^0_S mesons is performed using the most abundant decay mode, which is $K^0_S \to \pi^+\pi^-$. A sketch of the entire decay chain can be seen in Figure 2.3. Hereinafter, when mentioning $D^{*+} \to D^0\pi^+$ decays, it incorporates the charge conjugated process, $D^{*-} \to \bar{D}^0\pi^-$, as well.

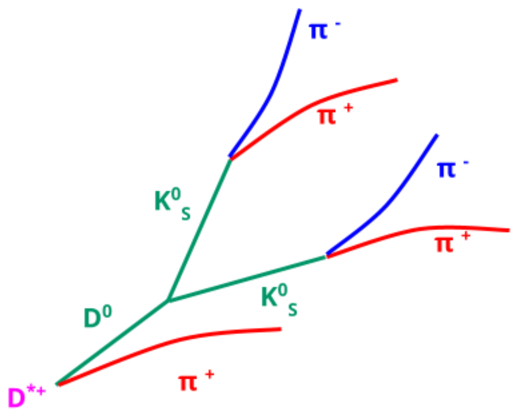

Figure 2.3: Schematic representation of the decay chain. Typical decay lengths are not to scale. The charge tracks used to reconstruct the decay are the ones in red and blue, while neutral particles are in green [2].

2.3 Current state of the CP asymmetry measurement in $D^0 \to K^0_S K^0_S$ decays

The value of the CP asymmetry in the $D^0 \to K^0_S K^0_S$ decay channel has been theoretically predicted as well as experimentally measured.
The current theoretical prediction based on the SM [1] states

$$A^{\mathrm{CP}}(D^0 \to K^0_S K^0_S) \leq 1.1\% \text{ at } 95\% \text{ C.L.}$$

for the CP asymmetry in the decay. However, the result could be enhanced due to the interference with additional diagrams featuring beyond SM contributions.
To experimentally verify the theoretical prediction, the measurement has been carried out by the Belle and the LHCb experiment.
The Belle experiment [6, 7] has measured a CP asymmetry of

$$A^{\mathrm{CP}}_{\mathrm{Belle}}(D^0 \to K^0_S K^0_S) = (0.02 \pm 1.53 \pm 0.17)\%,$$

in the year 2017, where the first uncertainty is statistical and the second uncertainty is systematic. With the Belle II upgrade it is expected that the amount of data collected would be increased from 921 fb^{-1} to 50 ab^{-1}. Thus, the statistical uncertainty is predicted to be reduced to 0.2%.
The current most precise measurement of the CP asymmetry in the $D^0 \to K^0_S K^0_S$ decay has been carried out by the LHCb experiment with Run 2 data [2] resulting in

$$A^{\mathrm{CP}}_{\mathrm{LHCb}}(D^0 \to K^0_S K^0_S) = (-3.1 \pm 1.2 \pm 0.4 \pm 0.2)\%,$$

where the first uncertainty is statistical, the second systematic, and the third is due to the uncertainty on the asymmetry of the calibration channel.

Chapter 3

The LHCb experiment

The LHCb experiment, located at the Large Hadron Collider (LHC), is specifically designed to study bottom and charm decays to probe the SM of particle physics and search for beyond SM phenomena. The acronym LHCb stands for LHC *beauty*, referring to its focus on the beauty quark during the early stages of its existence. LHCb has been operating since 2010 during the data-taking periods Run 1 (2010-2012), Run 2 (2015-2018) and currently in Run 3 (2022-2025). With the start of Run 3, the instantaneous luminosity increased by a factor of 5 from $4 \times 10^{32}\ \text{cm}^{-2}\text{s}^{-1}$ to $2 \times 10^{33}\ \text{cm}^{-2}\text{s}^{-1}$.

3.1 The Large Hadron Collider

The LHC [8] is a proton-proton and heavy ion collider at the European Organization for Nuclear Research (CERN) laboratory, located on the French-Swiss border near Geneva. The LHC consists of a 26.7 km long ring where two beams of protons or ions are accelerated in opposite directions and brought to collision at four distinct points. These collision points house the four major experiments of the LHC: ATLAS and CMS for general-purpose research, ALICE for heavy ion studies and LHCb, a spectrometer focused on flavour physics. The LHC is capable of achieving centre-of-mass energies, E_{cms}, up to 13.5 TeV.

3.2 The LHCb detector

The LHCb detector [9] is a single-arm forward spectrometer which covers a pseudorapidity η range of $2 < \eta < 5$. The pseudorapidity is defined as $\eta = -\log[\tan(\theta/2)]$ where θ is the polar angle with respect to the beam direction. The coordinate system used has the origin at the proton-proton interaction point, the z axis is aligned with the proton beam and pointing towards the muon system, the y axis pointing upwards and the x axis defining a right-handed system. Figure 3.1 shows the detector layout used for Run 3.

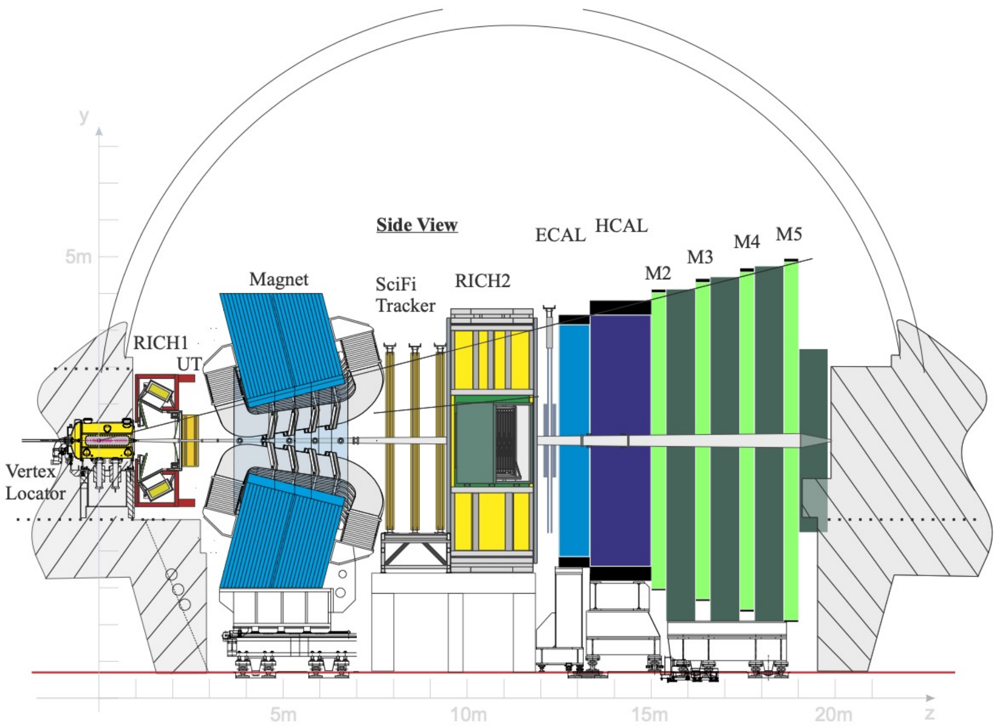

Figure 3.1: Layout of the LHCb detector for Run 3 [9].

3.2.1 Tracking detectors

The tracking system must provide accurate spatial measurements of the trajectories of charged particles, in order to determine their charge, momenta and vertex positions. Therefore, the particle tracking system comprises of a silicon pixel detector surrounding the interaction region known as the Vertex Locator, the silicon-strip based Upstream Tracker located upstream of the dipole magnet, and the Scintillating Fibre Tracker stations positioned downstream of the magnet. To meet the requirements of Run 3, all these subdetectors are compatible with the increased instantaneous luminosity and the triggerless 40 MHz readout.

Vertex Locator

The Vertex Locator (VELO) [9, 10] is stationed around the collision region and is responsible for detecting tracks of ionizing particles which originate from the beam collision. It accurately measures the primary vertex position (PV) and the impact parameter (IP), which is defined as the smallest distance from a particle trajectory to the PV. The VELO tracks serve as seeds for the reconstruction algorithm of the LHCb spectrometer and provide valuable discriminatory information for event selection.

The dipole magnet

The spectrometer utilizes a dipole magnet which facilitates the bending of particles for momentum measurements. This magnet generates a vertical magnetic field with a bending power of ≃ 4 Tm. To ensure balanced data collection, the magnet polarity is regularly reversed during data taking, resulting in approximately equal-sized data sets with the two field configurations.

Upstream Tracker

The Upstream Tracker (UT) [9, 11] is positioned upstream of the magnet. Its main purpose is to track charged particles and it plays a crucial role in the initial processing algorithm of the software trigger. By combining the tracks obtained from the VELO and UT, along with the stray magnetic field, a preliminary determination of the track momentum p is achieved with a precision of $\sim 15\%$ [9]. Moreover, the momentum measurement allows the determination of the particle's charge, reducing the time required by the forward tracking algorithm.

Scintillating Fibre Tracker

The Scintillating Fibre (SciFi) Tracker [9, 11] is positioned downstream of the magnet and is in charge of reconstructing tracks of charged particles. Together with measurements of VELO and UT upstream of the magnet, the SciFi Tracker contributes to the determination of the particle's momentum with high precision.

3.2.2 Particle identification

The particle identification system consists of two Ring Imaging Cherenkov detectors, two calorimeters and the muon stations at the end of the detector. Its goal is to formulate hypotheses about the type of particle which transverses through the detectors. The Cherenkov detectors are capable of distinguishing between charged kaons, pions and protons, while the calorimeters allow for the identification of electrons, photons and hadrons. Lastly, the muon chambers identify the muons.

Ring Imaging Cherenkov detectors

Two Ring Imaging Cherenkov (RICH) detectors, RICH1 and RICH2 [9], facilitate the discrimination of charged hadrons, specifically the separation between pions, kaons and protons, across a momentum spectrum spanning from 2.6 to 100 GeV/c. By utilizing the Cherenkov effect, the velocity of the particle can be estimated. Together with the momentum derived from the tracking system, the mass and thus the particle can be identified.
In particular, RICH1 is designed to identify particles within the momentum range of 2.6 to 60 GeV/c, utilizing a C_4F_{10} gas radiator. On the other hand, RICH2 employs CF_4 as a gas radiator to identify high-momentum particles ranging from 15 to 100 GeV/c. RICH1 is located upstream of the magnet between the VELO and the UT, while RICH2 is located downstream of the magnet after the SciFi. In Figure 3.2 the relation between the Cherenkov angle and particle momentum is shown for different particles with the C_4F_{10} radiators.

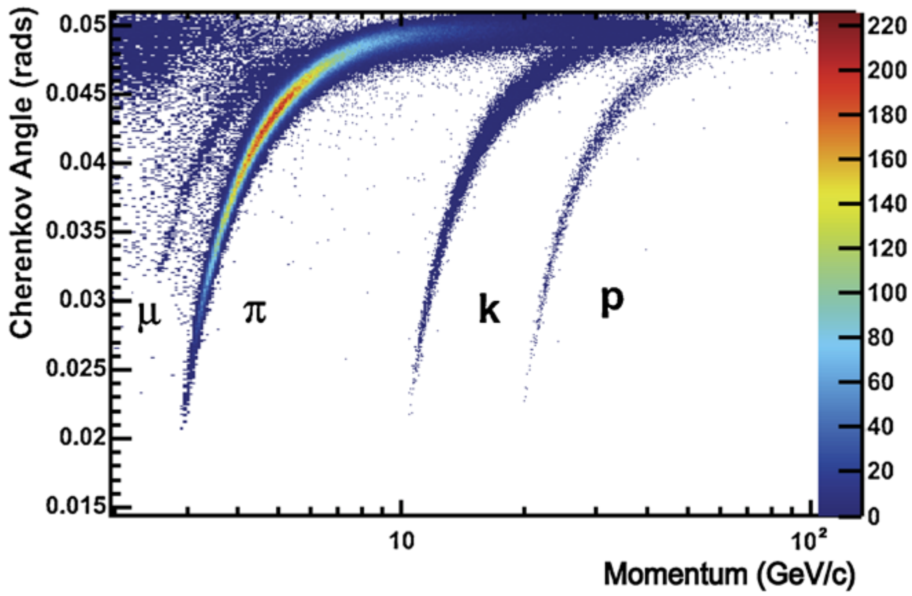

Figure 3.2: Reconstructed Cherenkov angle as a function of track momentum in the C_4F_{10} *radiator [12].*

Calorimeter detector

The calorimeter system [13] consists of the electromagnetic calorimeter (ECAL) as well as the hadronic calorimeter (HCAL), positioned after the RICH2 detector. It serves as a particle identifier for electrons, photons and hadrons and the measurement of their energy and position.

Muon chamber

The Muon detector [9] consists of four stations (M2 - M5) which are positioned after the calorimeter system. These detectors are designed to provide identification and transverse momentum measurements of penetrating muons.

3.2.3 Trigger system

With the information obtained from all detection systems, the entire decay chain leading up to the *pp* collision of an event can be reconstructed. However, not all events are considered valuable, and it is not feasible to store all the information. The trigger-less readout of the detectors operates at a rate of 40 MHz, but for non-empty bunch crossings, it is reduced to 30 MHz. In order to reduce the rate to a manageable level for storage, a two-stage software trigger known as the high level trigger (HLT) is performed. The outline of the trigger system is presented in Figure 3.3. The first stage of the trigger reduces the rate from 30 MHz to 1 MHz by performing a partial reconstruction of the tracks. Subsequently, the event rate is further reduced to a few kHz in the second stage through a complete reconstruction and event selection process.

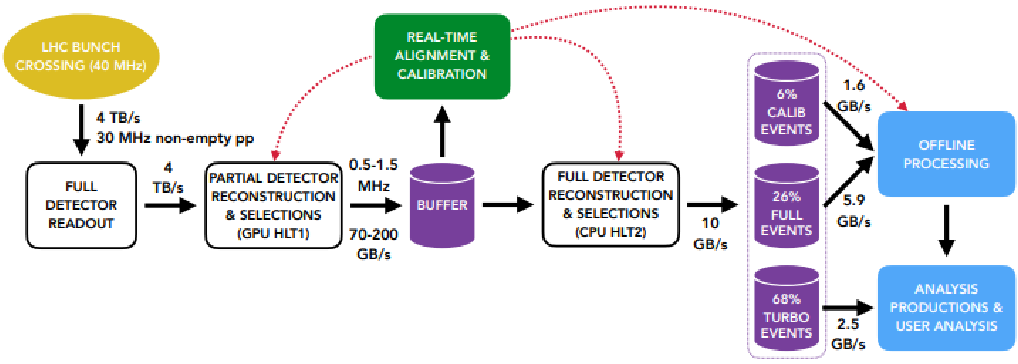

Figure 3.3: Online data flow [14].

High level trigger 1

The first stage, known as the high level trigger first stage (HLT1) [9], is responsible for reducing the event rate from 30 MHz to 1 MHz. The reconstruction process begins by considering the tracks inside the VELO, which are reconstructed as straight lines due to the negligible magnetic field in that region. Using this information, the primary vertex can be determined by extrapolating the tracks within the VELO. By incorporating the information from the UT hits, an initial estimation of the momentum is performed, taking the stray magnetic field into account. With the magnetic field, the tracks are extrapolated to the SciFi, where a more precise momenta estimation is performed. Therefore, HLT1 triggers only on particles which traverse through the full tracking system. Finally, a Kalman filter is applied to provide a good estimation of the χ^2_{IP} of the tracks.
Based on the reconstructed track and vertex information, several selection criteria are applied, referred to as the HLT1 trigger lines. Events which pass the trigger selection are stored in a buffer and subsequently passed to the second stage for further selection.

High level trigger 2

The second stage of the trigger system, known as the high level trigger second stage (HLT2) [9], is responsible for reducing the event rate from 1 MHz to a few kHz. The buffer allows the HLT2 stage to have more time to process the data and perform a complete reconstruction using all the information provided by the detectors. During this stage, selection criteria called HLT2 trigger lines are applied to the fully reconstructed data. The trigger lines are designed to select events which are of interest for the analysis and filter out background events.

3.2.4 Track reconstruction

Trajectories of charged particles, called tracks, are reconstructed using the hits from the subdetectors. Different types of tracks are distinguished according to the subdetectors crossed, as shown in Figure 3.4:

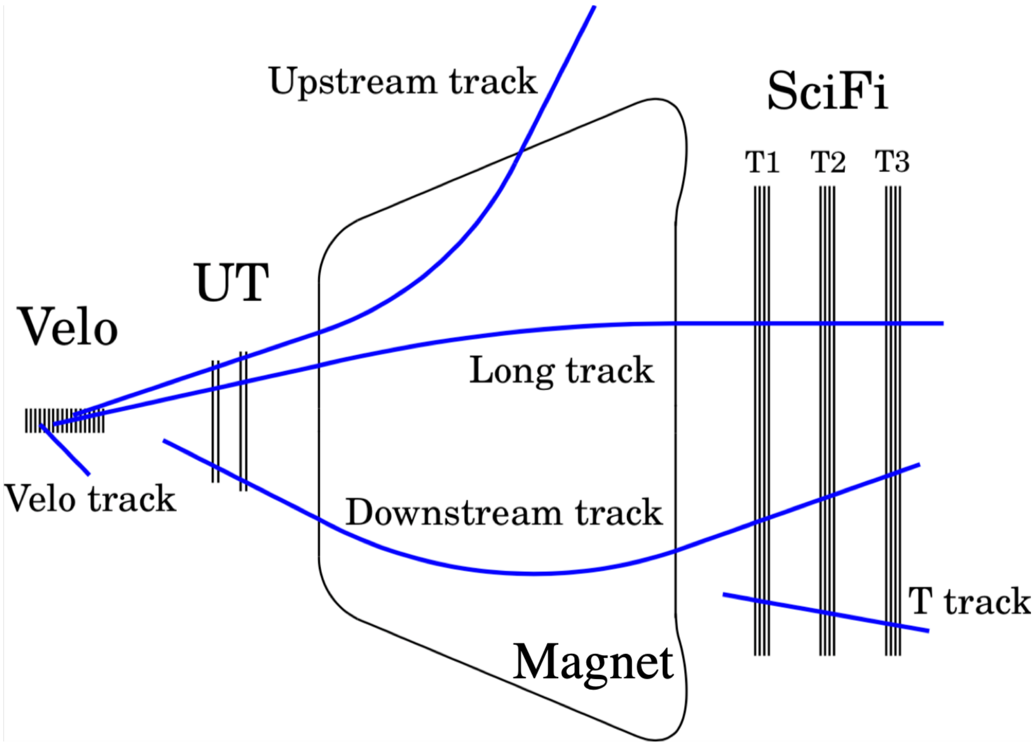

Figure 3.4: Track types in the LHCb detector bending plane. Adapted from [9].

- **Long tracks (L)** require particles to cross the full tracking system and leave hits in all subdetectors.
- **Downstream tracks (D)** are reconstructed using hits in the UT and SciFi Tracker. These particles most likely originate from the decay of long-lived particles outside of the VELO acceptance region, e.g. from the decay of a K^0_S.
- **Upstream tracks (U)** are low momentum particles which leave hits in the VELO and UT but are swept out of the LHCb acceptance by the magnetic field.
- **Velo tracks** only have hits inside the VELO and are used to determine the position of the primary *pp* collisions, a process known as primary vertex finding.
- **T tracks** are only formed using hits from the SciFi Tracker.

3.3 Monte Carlo simulations

The study presented in this thesis is based on Monte Carlo (MC) [13] simulations. MC simulations involve the random generation of data which aim at replicating the behaviour of data obtained through experiments. To meet these requirements, two packages from the LHCb software are employed: Gauss [15] and Boole [16].
Gauss oversees the generation of the initial particles and the simulation of their transport through the LHCb detector. The simulation of the initial *pp* collision is carried out by the MC event generator Pythia [17]. The subsequent decays and time evolution of particles

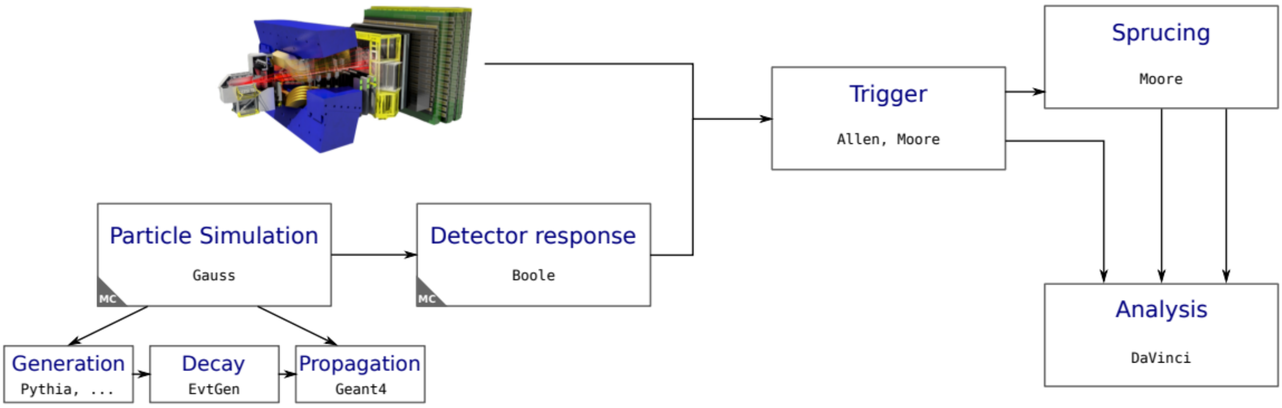

Figure 3.5: Schematic representation of the LHCb upgrade data flow and the related LHCb application, with an emphasis on simulation [13].

produced in the PYTHIA step are delegated to the EVTGEN [18] framework. Afterwards, the GEANT4 [19] toolkit is responsible for simulating the physical processes which the particles undergo as they traverse the detector.
The BOOLE program replicates the various responses of the subdetectors to hits and performs digitization, converting the data into the same format as that provided by the experimental electronics. The resulting files are referred to as MC simulations in Digi format.

After digitization, real data and MC follow the same processes. The HLT reconstruction and selection are carried out by the MOORE framework. The complete data flow for MC simulations is depicted in Figure 3.5.

Chapter 4

Overview of the analysis

The goal of this analysis is to increase the obtained yields per unit of luminosity in $D^0 \to K^0_S K^0_S$ decays. To achieve this, different track types for the reconstruction of the decay channel are considered due to the topology of the $D^{*+} \to D^0(K^0_S K^0_S)\pi^+$ decay. The K^0_S mesons stemming from this decay are produced with a boost factor of $\langle \beta\gamma \rangle \sim 40$ [2] (γ being the Lorentz factor and $\beta = v/c$) in the beam direction. With an average lifetime of $\tau = (0.89564 \pm 0.00033) \times 10^{-10}$s [5], it results in a mean decay length of $\langle \beta\gamma c\tau \rangle \sim 1.1$ m. Thus, it can be estimated that around 37% of the decays occur inside the VELO acceptance, 50% between the VELO and UT, and the remaining 12% decay after the UT. The decays occurring after the UT are deemed unusable due to the inability to determine their momenta. Therefore, the majority of K^0_S decays happen outside the VELO acceptance, which is the LHCb subdetector with the most precise hit resolution. This results in a highly inefficient selection at the trigger level, which will be further discussed in Chapter 6. As a result, the $D^0 \to K^0_S K^0_S$ decay is constrained by the available statistics.

To enhance the accuracy of the measurement by reducing the statistical uncertainty, the inclusion of upstream tracks — alongside long and downstream tracks — is considered to increase the yields per unit of luminosity. Consequently, the different properties of the pions, determined by their track types, lead to the distinction of the following types of K^0_S:

- The $\boldsymbol{K^0_{S\,\mathrm{LL}}}$ decays inside the VELO acceptance and the daughter pions intersect all the tracking stations. Therefore, both pions are reconstructed from long tracks;
- The $\boldsymbol{K^0_{S\,\mathrm{LD}}}$ decays inside the VELO acceptance. While one pion is reconstructed from a long track, the second one is reconstructed from a downstream track;
- The $\boldsymbol{K^0_{S\,\mathrm{DD}}}$ decays outside the VELO acceptance. Hence, both daughter pions are reconstructed from downstream tracks, using the UT and SciFi hit information;
- The $\boldsymbol{K^0_{S\,\mathrm{UL}}}$ decays inside the VELO acceptance. One pion is reconstructed as a long track, while the second one is swept out by the magnet and classified as upstream.

By utilizing these four types of K^0_S, the D^0 candidates can be labelled as XXYY, where XX and YY represent the track type of the daughter pions of the first and second K^0_S, respectively.

Therefore, the LLLL, LLLD, LLDD, LDDD, DDDD, ULLL and ULDD samples are considered. Only the LLLL, LLDD and DDDD samples have already been used in previous analyses. Thus four additional combinations are considered while other combinations are disregarded due to low statistics. Furthermore, the long track type of the π_{soft} is indicated using the subscript "L".

Results obtained during Run 2 measurement

The yields used for the CP asymmetry measurement in $D^0 \to K_S^0 K_S^0$ decays obtained from Run 2 data are reported in Table 4.1. Upon comparing the yields, it becomes evident that the DDDD_L sample is eight times smaller than the LLLL_L sample, despite an expected ratio based on the geometrical acceptance of

$$\text{LLLL}_\text{L} : \text{LLDD}_\text{L} : \text{DDDD}_\text{L} = 1 : 2.7 : 1.9. \tag{4.0.1}$$

The observed discrepancy between the obtained yields and the geometrical acceptance is due to the inefficient selection of downstream tracks during trigger level, which will be further discussed in Chapter 6. A significant amount of effort has already been dedicated to incorporating the DDDD_L sample in past analyses, despite its relatively minor impact. Therefore, this sample has been chosen as the baseline for evaluating the inclusion of other samples in this analysis.

Table 4.1: Yields in the individual samples used for the Run 2 analysis [2].

	2017 + 2018	2015 + 2016
sample	Yield	Yield
LLLL_L	4056 ± 77	1388 ± 41
LLDD_L	1145 ± 49	411 ± 25
DDDD_L	87 ± 28	-

4.1 Impact on mass resolution using upstream tracks

To extract the yields of D^0 and $\overline{D}^0$ decays a multidimensional maximum-likelihood fit is performed on the $\Delta m \equiv m(D^*) - m(D^0)$ and the mass distribution of both K_S^0. Using a multi-dimensional fit physical background such as the $D^0 \to K_S^0 \pi^+ \pi^-$ decays can be disentangled from the signal. Hence, similar resolutions in the Δm distribution of the additional samples compared to the DDDD_L sample are required to consider them as candidates for inclusion in the analysis. If the Δm distribution has a significantly worse resolution, distinguishing between signal and background may not be possible.

The mass distribution of the K_S^0 is modelled using a single Gaussian probability density function (PDF). The outcomes for the $K_{S\,\text{LL}}^0$ and $K_{S\,\text{UL}}^0$ distributions are depicted in Figure 4.1,

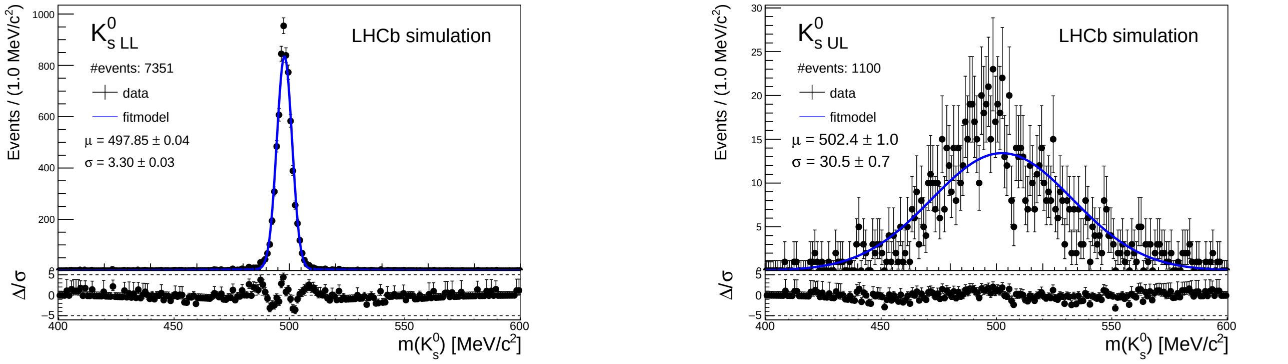

Figure 4.1: K^0_S mass distributions. Left for K^0_S reconstructed from two long tracks. Right for K^0_S reconstructed from one long and one upstream track.

while in Appendix A the fits for all the different K^0_S mass distributions are reported. Both distributions peak at the same mass value, but the K^0_S mass distribution for $K^0_{S\,\mathrm{UL}}$ has a width that is ten times larger than that for $K^0_{S\,\mathrm{LL}}$ due to the poor momenta measurement of upstream tracks with a precision of ~ 15%. However, the worse resolution of the K^0_S mass distribution does not prove to be a significant issue for the analysis, as the yields for the CP asymmetry measurement are primarily extracted from the Δm distribution.

The Δm distribution is described using the Johnson S_{U} distribution [20]

$$j(x) \propto \frac{\delta}{\lambda\sqrt{2\pi}} \frac{1}{\sqrt{1+\left(\frac{x-\mu}{\lambda}\right)^2}} \exp\left[-\frac{1}{2}\left(\gamma + \delta \sinh^{-1}\left(\frac{x-\mu}{\lambda}\right)\right)^2\right]. \tag{4.1.1}$$

Considering the definition of the Johnson S_{U} distribution, no single variable effectively captures the width. Therefore, the full width at half maximum (FWHM) parameter is employed to assess the feasibility of inclusion. In Figure 4.2, exemplary, the Δm distributions for the $\mathrm{LLLL_L}$ and $\mathrm{ULLL_L}$ samples are shown with FWHM values of 1.153 MeV/c^2 and 1.261 MeV/c^2, respectively. Due to the momenta measurement with a precision of ~ 15% utilizing the VELO and UT for upstream tracks, an increase in the FWHM of 9% between these samples is observed.

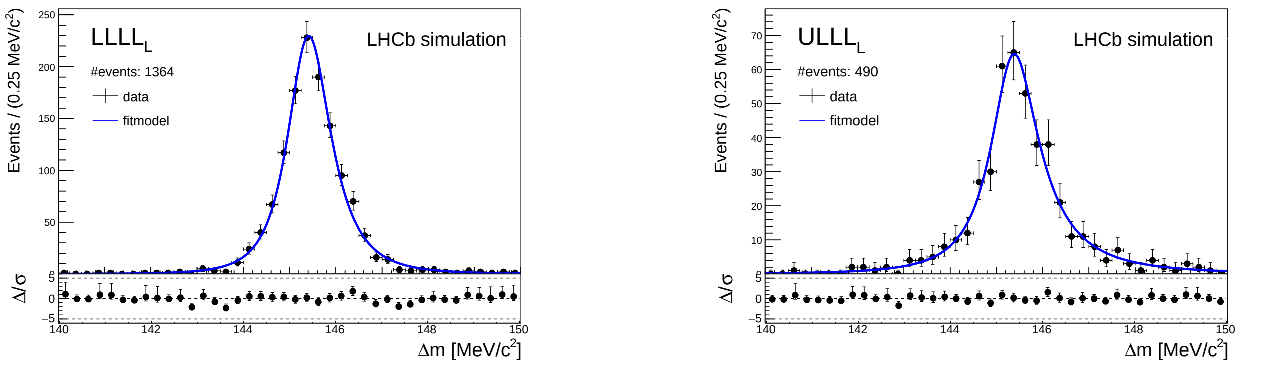

Figure 4.2: Δ m distribution. Left for the $\mathrm{LLLL_L}$ sample. Right for the $\mathrm{ULLL_L}$ sample.

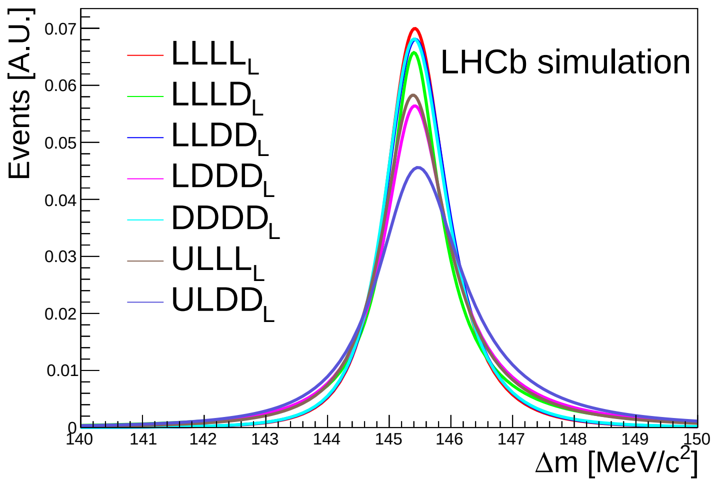

Figure 4.3: Normalized Δm distributions of all samples.

Table 4.2: FWHM values of all samples.

sample	FWHM [MeV/c^2]
$\mathrm{LLLL_L}$	1.153
$\mathrm{LLLD_L}$	1.028
$\mathrm{LLDD_L}$	1.185
$\mathrm{LDDD_L}$	1.264
$\mathrm{DDDD_L}$	1.177
$\mathrm{ULLL_L}$	1.261
$\mathrm{ULDD_L}$	1.647

The results for all performed fit with their corresponding parameters are reported in Appendix B. In Figure 4.3 the normalized fit function of all samples are shown, whereas in Table 4.2 the corresponding FWHM values are reported. Based on these results, the FHWM parameter of all samples is similar, except for the $\mathrm{ULDD_L}$ sample. For the $\mathrm{ULDD_L}$ sample an increase in its FWHM of 43% is observed compared to the $\mathrm{LLLL_L}$ sample. However, the resolution of the Δm distribution is still sufficient for extracting the yields which also holds for the other samples.

In the case of an even worse resolution, the ability to differentiate between signal and background is expected to diminish. As a result, only samples with one upstream track and the rest consisting of long or downstream tracks are under consideration. This configuration ensures a reasonable resolution for the Δm distribution, a requirement for effective background rejection. If a sample involves more upstream tracks, a substantial decrease in resolution would be anticipated. In Figure 4.4 the distribution of the $\mathrm{ULUL_L}$ sample is shown with a FWHM twice as large as the $\mathrm{LLLL_L}$ sample. Thus deeming the $\mathrm{ULUL_L}$ samples unusable.

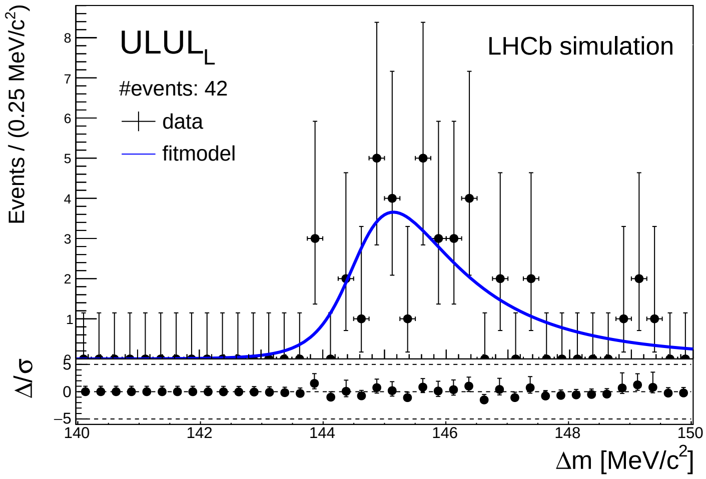

Figure 4.4: Δm distribution of the ULUL$_\mathrm{L}$ sample.

Chapter 5

Trigger selection

In addition to attaining a comparable resolution in the Δm distribution, it is necessary for the samples containing upstream tracks to be selectable during the trigger stage. If this is deemed feasible, a dedicated HLT2 trigger line to select the $D^0 \rightarrow K_S^0 K_S^0$ decays is necessary.

5.1 Background analysis for K_S^0 using upstream track

A prominent background source comes from random combinations of pions, wrongly identified as the decay products of a K_S^0. In particular, the case of the $K^0_{S\,\mathrm{UL}}$ is of interest because the other samples have already been analyzed in the past [2].
To mitigate this background, MC simulations for K_S^0 coming from $D^0 \rightarrow K_S^0 K_S^0$ decays and pions from minimum bias events are employed.
To effectively distinguish between the signal and background, the $\chi^2_{\mathrm{min}}(\pi) \equiv \min(\chi^2_{\mathrm{IP}}(\pi_{\mathrm{U}}), \chi^2_{\mathrm{IP}}(\pi_{\mathrm{L}}))$ and the transverse momentum of the K_S^0 variables are exploited. The Impact Parameter (IP) refers to the distance between the track trajectory and the PV, whereas χ^2_{IP} is defined as the χ^2 of the primary vertex fit with and without considering the particle in the fit.
The considered background events consist of pions originating directly from the *pp* collision, which lead to a small $\chi^2_{\mathrm{min}}(\pi)$ value with a mean of 3. In the case of the signal events, the pions originate from the decay vertex of the K_S^0, resulting in a displacement due to the long flight distance of the K_S^0. Thus leading to a significantly higher $\chi^2_{\mathrm{min}}(\pi)$ value, with a mean of 1163. Furthermore, the K_S^0 originating from the $D^* \rightarrow D^0(K_S^0 K_S^0)\pi$ decay are produced with a boost, resulting in higher transverse momentum values.
By employing the rectangular cut module in the TMVA package [21] to optimize the selection, the results are visible in the receiver operating characteristic (ROC) curve in Figure 5.1. This curve demonstrates that high background rejection is achievable throughout the entire signal efficiency range. In Figure 5.2, the distribution of $\chi^2_{\mathrm{min}}(\pi)$ against $p_{\mathrm{T}}(K_S^0)$ for both signal and background events is shown. Additionally, the cuts for a 96% signal efficiency with a 99% background rejection are depicted. It is evident that the majority of background events have lower $\chi^2_{\mathrm{min}}(\pi)$ values than the selected threshold, whereas the majority of signal events lie above the cut.

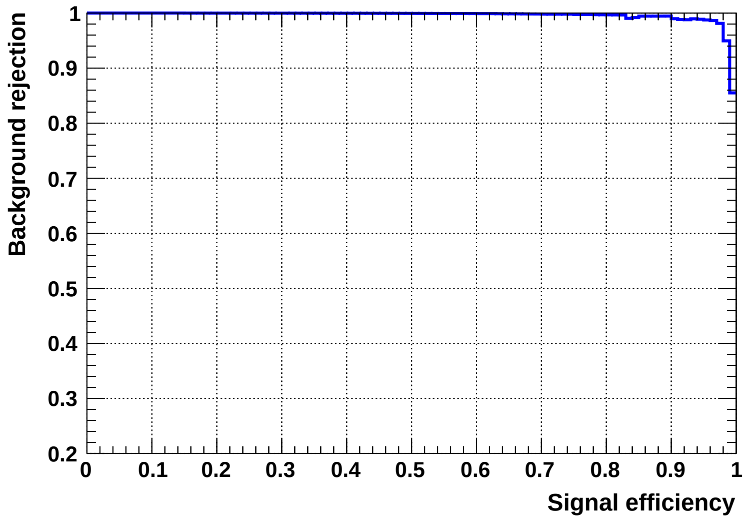

Figure 5.1: ROC curve of the TMVA output showing the background rejection against the signal efficiency.

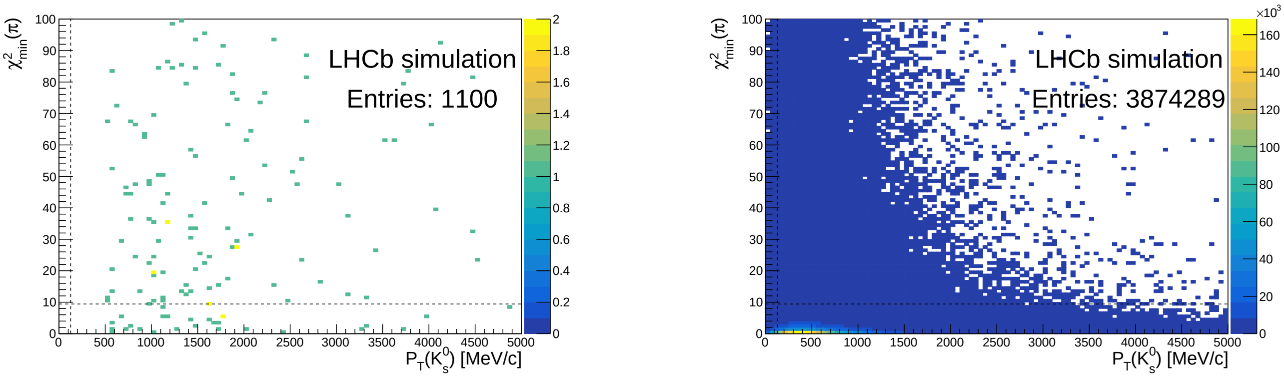

Figure 5.2: $\chi^2_{\mathrm{min}}(\pi)$ against the $p_{\mathrm{T}}(K^0_S)$ distribution for signal (left) and background (right). The dotted line represents the cuts required for the 96% signal efficiency with a 99% background rejection. For the signal, the majority of the events lie beyond the range of the graph and are not affected by the cuts.

5.2 Selection at first stage of high level trigger

The first trigger line, HLT1, utilizes tracks reconstructed inside the VELO detector to identify decays of B or D mesons. However, at this stage, triggering is only performed on long tracks, which poses an issue for $D^0 \to K^0_S K^0_S$ decays as the majority of the K^0_S decay outside of the VELO acceptance and are therefore only reconstructable with downstream track pions.
The triggering of events at the HLT1 level can be categorized into two types based on tracks or combinations of tracks:

- **Trigger On Signal (TOS)** events: These events are triggered by the signal of the decay chain, regardless of the presence of other tracks. This takes place when the reconstructed signal satisfies the selection criteria of the respective trigger line.

- **Trigger Independent-of-Signal (TIS)** events: These events are triggered independently of the signal's presence. A candidate is considered TIS with respect to a trigger selection if removing it from the event would still cause the trigger selection to accept the event, i.e. if the other particles in the event are sufficient to satisfy the trigger selection.

Therefore, it is still possible to retrieve downstream tracks using TIS events, even when no direct triggering is performed. The trigger lines used in the selection are the `HLT1TrackMVA` and the `HLT1TwoTrackKsMVA`, which is dedicated to trigger K_S^0. During this trigger stage, a partial reconstruction is performed for charged particles and the K_S^0. The D^* and D^0 are not reconstructed during this stage.

5.3 Selection at second stage of high level trigger

During the HLT2 trigger stage, a full reconstruction is performed. Thus the samples are selected with separate trigger lines due to their different properties. Additionally, the trigger line is required to reduce the input rate from 1 MHz to a few kHz. Hence, harsh cuts are necessary to fulfil the demands.
The K_S^0 candidates are reconstructed from the $K_S^0 \to \pi^+\pi^-$ decay mode, where the π is either reconstructed as a long (π_{L}), downstream (π_D), or upstream (π_U) track. To select these pions the selection criteria derived from the past analysis [2] and the results of the background analysis (Section 5.1) are used. In Table 5.1 the requirements for the different track type pions are depicted.

Table 5.1: HLT2 reconstruction selection cuts for π from K_S^0 decays; in brackets are the cuts on the daughter π_D from $K^0_{S\,\mathrm{LD}}$ decays.

Variable	π_L	π_D	π_U
$\chi^2_{\mathrm{IP}}(\pi)$	> 36	-	> 10
$p_{\mathrm{T}}(\pi)$	-	> 175 (100) MeV/c	-
$p(\pi)$	-	> 3000 (2000) MeV/c	-

Additionally, harsh cuts are applied on upstream track particles at the reconstruction level, due to the constraint on the total computational time given by the finite computing resources of the HLT2 trigger. It currently incorporated the following requirements on the momenta of upstream particles which are referred to as "reconstruction cut":

$$p(\pi_{\mathrm{U}}) = 1500\ \mathrm{MeV/c} \qquad \text{and} \qquad p_{\mathrm{T}}(\pi_{\mathrm{U}}) = 300\ \mathrm{MeV/c} \tag{5.3.1}$$

At this trigger stage, two pairs of π with an invariant mass compatible with the K_S^0 mass are selected. Moreover, if the K_S^0 is reconstructed from at least one long or upstream track, it is required to decay inside the VELO acceptance. However, in the case of $K^0_{S\,\mathrm{DD}}$ the endvertex could be in the final part of the VELO or outside its acceptance but before the UT. If the K_S^0 decays inside the VELO both π should theoretically be classified as long tracks, but it is possible that the π leaves insufficient hits inside the VELO and hence these pions are labelled as downstream tracks. In addition, a cut on the transverse momentum and the $\chi^2_{\mathrm{vtx}}/\mathrm{ndf}$ of the K_S^0 is imposed. The $\chi^2_{\mathrm{vtx}}/\mathrm{ndf}$ is defined as the χ^2 value of the endvertex normalized to the number of degrees of freedoms. The detailed cuts on the K_S^0 are listed in Table 5.2. Furthermore, the invariant mass of the K_S^0 pair is required to lie within a certain mass range of the D^0.

The selection of D^*, D^0 and π_{soft} is independent of the track types of the K_S^0 decay. Additionally, the selection criteria induced by the calibration channel $D^0 \to K^+K^-$ have to be incorporated into the trigger line to correct for detection and production asymmetry, as well as the inclusion of secondary decays. These induced cuts from the calibration channel are on the momenta of the π_{soft} and the $\chi^2_{\text{vtx}}/\text{ndf}$ of the D^0. The complete selection of the $D^0 \to K_S^0 K_S^0$ and the $D^* \to D^0\pi_{\text{soft}}$ candidates can be found in Table 5.3.

Table 5.2: HLT2 reconstruction selection for K_S^0; in brackets for $K^0_{S\,\text{LL}}$ in the ULLL sample.

Variable	$K^0_{S\,LL}$	$K^0_{S\,DD}$	$K^0_{S\,LD}$	$K^0_{S\,UL}$
$\chi^2_{\text{vtx}}/\text{ndf}(K_S^0)$	< 7	< 10	< 10	< 10
$p_{\text{T}}(K_S^0)$	$> 500\ (300)$ MeV/c	> 500 MeV/c	> 500 MeV/c	> 400 MeV/c
$z(K_S^0)$	$\in [-100, 500]$ mm	$\in [300, 2275]$ mm	$\in [50, 500]$ mm	$\in [-100, 500]$ mm
$\lvert m(\pi\pi) - m(K_S^0)\rvert$	< 30 MeV/c^2	< 60 MeV/c^2	< 65 MeV/c^2	< 70MeV/c^2

Table 5.3: HLT2 reconstruction selection for D^0, D^* and π_{soft}. Cuts induced from the calibration channel in blue, are referred to as calibration channel cuts.

Variable	LLLL	LLLD	LLDD	LDDD	DDDD	ULLL	ULDD
$\sum_{K_S^0} p_{\text{T}}$	> 1500 MeV/c						
$m(K_S^0 K_S^0)$	$\in [1775, 1955]$ MeV/c^2						
$\chi^2_{\text{vtx}}/\text{ndf}(D^0)$	< 10						
$m(D^*) - m(D^0)$	< 150MeV/c^2						
$\chi^2_{\text{vtx}}/\text{ndf}(D^*)$	< 25						
$p_{\text{T}}(\pi_{\text{soft}})$	> 200 MeV/c						
$p(\pi_{\text{soft}})$	> 1000 MeV/c						

5.3.1 Momentum and transverse momentum cut of the HLT2 trigger line

The current HLT2 trigger line incorporates two harsh cuts for the event selection. The first cut is the selection requirements stemming from the calibration channel. In Figure 5.3 the momenta distributions for the long track π_{soft} of MC simulation are shown. Additionally, the cuts induced from the calibration channel are depicted as well. Consequently, the transverse momentum cut proves to be an issue as it is positioned at the peak of the distribution, resulting in a significant signal loss of $(39.12 \pm 0.04)\%$. In contrast, the momentum cut does not affect the distribution at all.

The second harsh cut in the HLT2 trigger is the reconstruction cut (eq. (5.3.1)) targeted at the upstream particle reconstruction. As a result, upstream particles with low momentum are never reconstructed. Considering the definition of upstream tracks, it is expected that

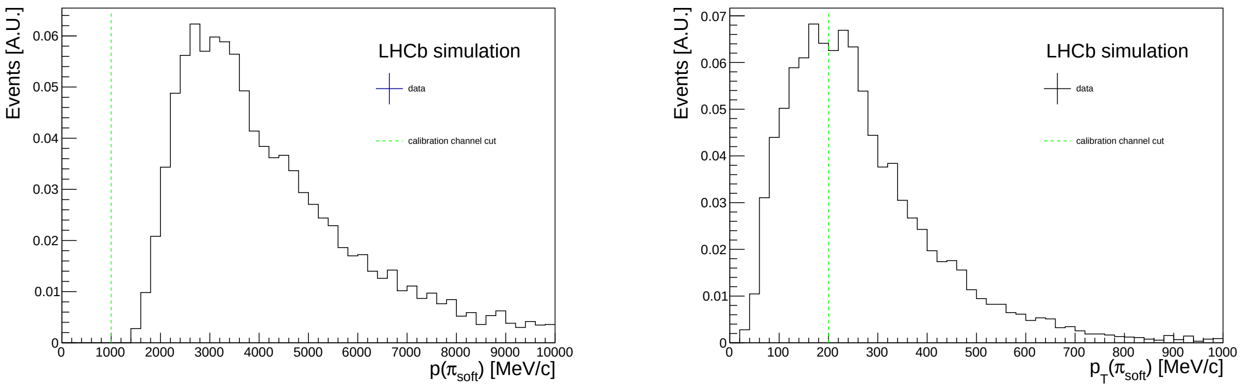

Figure 5.3: Momentum (left) and transverse momentum (right) distribution of the long track π_{soft}.

a significant amount is lost, as these upstream track particles possess low momentum, in order to bend out of the detector's acceptance range due to the magnet. In Figure 5.4a, the transverse momentum distribution of the upstream π from the ULLL_L and ULDD_L samples is shown, revealing a clear cutoff.

Utilizing the Moore framework it becomes possible to remove these constraints on the upstream reconstruction. Rerunning the reconstruction process without the reconstruction cut reveals the transverse distributions of the upstream π depicted in Figure 5.4b and an increase of the yields by $(76 \pm 19)\%$ and $(63 \pm 16)\%$ for the ULLL_L and ULDD_L samples, respectively.

5.3.2 Efficiency of the trigger line

The HLT2 trigger lines have been tested on two data samples. The first data sample consists of generic *pp* collisions, which are referred to as minimum biased sample. This data sample has been processed by the HLT1 trigger and serves to determine whether the output rate of the developed HLT2 trigger satisfies the requirements of reducing the input rate. The obtained result yields a rate below 100 Hz, which represents the lowest possible rate achiev-

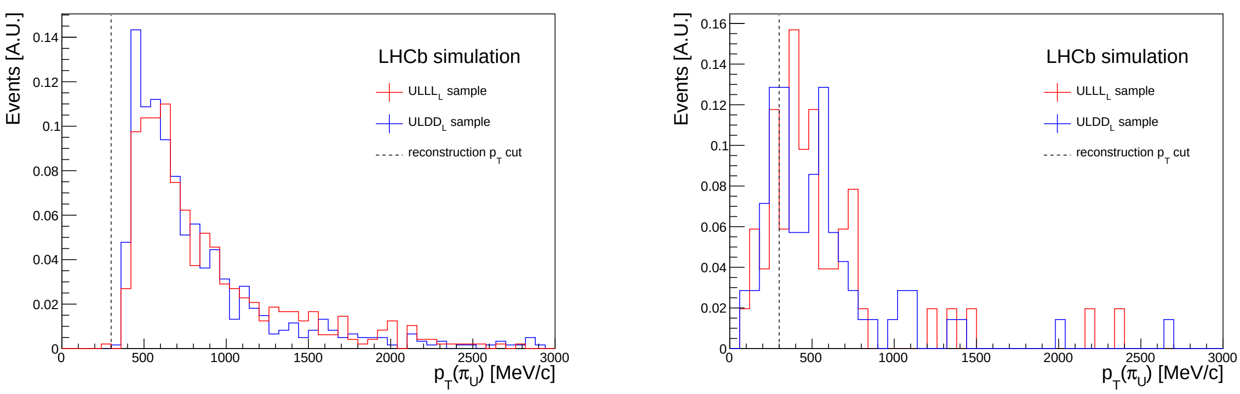

(a) with reconstruction cut. *(b) without reconstruction cut.*

Figure 5.4: Transverse momentum distribution of π_U for the ULLL_L and ULDD_L samples.

able with the currently available data, regardless of whether or not the reconstruction cut has been applied. Therefore, the rate is within the limits of the total HLT2 bandwidth that an HLT2 trigger line can have.

The second data set contains the MC simulations of $D^0 \rightarrow K_S^0 K_S^0$ events in Digi format. This data set is utilized to test the efficiency of the derived HLT2 trigger line, leading to the yields reported in Table 5.4, both without the application of the HLT1 trigger line and with and without the reconstruction cut. In addition, the yields obtained without any selection criteria except the reconstruction cut on the upstream track, which is referred to as "default selection", are reported as well. The obtained yields make it evident that the HLT2 trigger line reduces the yields by approximately a factor of ten compared to the default selection.

Table 5.4: Results of the HLT2 trigger line without HLT1 on MC simulations in Digi format.

	default selection	reconstruction cut	no reconstruction cut
$\mathrm{LLLL_L}$	1139	173	173
$\mathrm{LLLD_L}$	357	19	19
$\mathrm{LLDD_L}$	3397	431	431
$\mathrm{LDDD_L}$	561	23	23
$\mathrm{DDDD_L}$	2472	261	261
$\mathrm{ULLL_L}$	387	25	44
$\mathrm{ULDD_L}$	571	35	57

Until now, it has been shown that the analysis of the additional samples is possible due to their good resolution in the Δm distribution, as well as the selection at the HLT2 trigger level with decent efficiency, all while keeping the output rate of the trigger line at a desirable level. The impact on the sensitivity of the CP asymmetry measurement in $D^0 \rightarrow K_S^0 K_S^0$ decays by including the additional samples will be scrutinised in the next chapter.

Chapter 6

Sensitivity estimation

This analysis aims to assess the impact on the sensitivity in the CP asymmetry measurement of the $D^0 \to K_S^0 K_S^0$ decay channel by incorporating additional samples from different track types. The simplest approach would involve running both trigger lines (HLT1 and HLT2) over the MC sample and using the resulting numbers to determine the sensitivity of the measurement. However, this approach is not feasible given the limited size of the currently available MC samples. It is in fact expected that the number of events, which pass the HLT2 trigger, would be further reduced by a factor of 30 by the HLT1 trigger. Consequently, in certain samples, no event would survive the selection. Thus, the determination of the uncertainty utilizing this method would not be possible.
To still provide an estimation of the impact on the statistical uncertainty by the inclusion of additional samples, a more unconventional method has been chosen.

6.1 Methodology

The relative statistical uncertainty of the CP asymmetry measurement is asymptotically equal to the relative statistical uncertainty in the number of events

$$\sigma(A^{\mathrm{CP}}) \simeq \frac{\sigma(N)}{N} = \frac{1}{\sqrt{N}}. \tag{6.1.1}$$

To determine the number of events for each sample, both the HLT1 and HLT2 trigger lines are required to be taken into account. To correct for the HLT1 trigger selection, an efficiency approximation method has been chosen, while for the HLT2 trigger lines, the results from Table 5.4 are used.

During the HLT1 trigger stage, an event can be triggered either as TOS or TIS. TOS events can be triggered with the `HLT1TrackMVA` and `HLT1TwoTrackKsMVA` trigger lines. The `HLT1TrackMVA` triggers only on long tracks, therefore, an efficiency, ϵ, is assigned for each long track π within the sample. However, the trigger line does not fire on the π_{soft}. Triggering on the π_{soft} would introduce bias due to a trigger asymmetry based on electric charge. The π_{soft} carries a posi-

tive electric charge when tagging a D^0 and a negative charge when tagging a $\bar{D}^0$.
On the other hand, the `HLT1TwoTrackKsMVA` trigger line triggers only on K_S^0 with two long track daughter pions in a sample. However, the efficiency of this trigger line differs compared to the `HLT1TrackMVA`, thus, an efficiency ϵ' is assigned for each K^0_{SLL} in the sample.
Additionally, every event can be triggered as TIS, which has an efficiency five times smaller compared to a TOS event triggered with the `HLT1TrackMVA` trigger line. This has been estimated from the calibration channel $D^0 \to K^+K^-$ decay [2].
Therefore, the total efficiency can be calculated as follows:

$$\epsilon_{\mathrm{sample}} = \#\, \pi_{\mathrm{L}} \text{ in sample} \cdot \epsilon + \#\, K^0_{\mathrm{SLL}} \text{ in sample} \cdot \epsilon' + 0.2 \cdot \epsilon. \tag{6.1.2}$$

However, the efficiencies of both HLT1 trigger lines are currently unknown. To provide a preliminary estimate, the `HLT1TwoTrackKsMVA` is initially disregarded, followed by presenting results that account for the trigger line. Through normalizing to the $\mathrm{LLLL_L}$ sample, the efficiency of the `HLT1TrackMVA` cancels out.

$$R = \underbrace{\frac{\epsilon_{\mathrm{sample}}}{\epsilon_{\mathrm{LLLL_L}}}}_{\mathrm{HLT1}} \cdot \underbrace{\frac{N_{\mathrm{sample}}}{N_{\mathrm{LLLL_L}}}}_{\mathrm{HLT2}}. \tag{6.1.3}$$

As a result, the corrected number of events are

$$N_{\mathrm{corr}} = R \cdot N_{\mathrm{LLLL_L}}. \tag{6.1.4}$$

The $\mathrm{DDDD_L}$ sample can only be triggered as a TIS event leading to an efficiency of $\epsilon_{\mathrm{DDDD_L}} = 0.2\epsilon$. In contrast, if the efficiency of the `HLT1TwoTrackKsMVA` trigger line is omitted, the efficiency of the $\mathrm{LLLL_L}$ sample is $\epsilon_{\mathrm{LLLL_L}} = 4.2\epsilon$. Thus based only on the HLT1 trigger the efficiency of the $\mathrm{DDDD_L}$ sample is a factor of 21 smaller compared to the $\mathrm{LLLL_L}$ sample. Considering, that the majority of the K_S^0 are decaying outside of the VELO acceptance, the HLT1 trigger is highly inefficient for selecting $D^0 \to K_S^0 K_S^0$ decays. Hence, leading to the limited available statistics.
This also applies to upstream tracks, which can not be triggered as a TOS event during the HLT1 trigger stage. Additionally, upstream tracks are affected by the reconstruction cut from the HLT2 trigger. These effects reduce the number of yields obtained in samples including upstream tracks significantly.

6.2 Results of the sensitivity estimation

To be able to determine the uncertainty utilizing this method the following assumptions are required:

1. The background is considered the same for all samples;

2. The values of ϵ and ϵ' and the ratio between them are currently still unknown. Therefore, the `HLT1TwoTrackKsMVA` is not considered, in order to be able to cancel out the efficiency by normalizing to the $\mathrm{LLLL_L}$ sample;
3. The number of events in the $\mathrm{LLLL_L}$ sample is considered to be 10000, which is the expected number obtainable during Run 3.

Employing these assumptions, the correct yields of each sample and their corresponding statistical uncertainty are reported in Table 6.1. The results are separated whether the reconstruction cut has been applied or not during the HLT2 trigger stage.

Table 6.1: Corrected yields of each sample with their corresponding relative statistical uncertainty with or without reconstruction cut.

	with reconstruction cut		without reconstruction cut	
sample	N_{corr}	$\sigma[\%]$	N_{corr}	$\sigma[\%]$
$\mathrm{LLLL_L}$	10000	1.0	10000	1.0
$\mathrm{LLLD_L}$	837	3.5	837	3.5
$\mathrm{LLDD_L}$	13050	0.9	13050	0.9
$\mathrm{LDDD_L}$	380	5.1	380	5.1
$\mathrm{DDDD_L}$	718	3.7	718	3.7
$\mathrm{ULLL_L}$	1101	3.0	1937	2.3
$\mathrm{ULDD_L}$	578	4.2	941	3.3

Leading to a ratio between the $\mathrm{LLLL_L}$, $\mathrm{LLDD_L}$ and $\mathrm{DDDD_L}$ sample of

$$\mathrm{LLLL_L} : \mathrm{LLDD_L} : \mathrm{DDDD_L} = 1 : 1.3 : 0.07 \tag{6.2.1}$$

while the analysis of Run 2 data (Table 4.1) resulted in a ratio of

$$\mathrm{LLLL_L} : \mathrm{LLDD_L} : \mathrm{DDDD_L} = 1 : 0.3 : 0.02. \tag{6.2.2}$$

Thus an improvement at the trigger level is observed. However, it is important to note, that the background, which augments with the number of downstream or upstream tracks in a sample, is not considered. Therefore, the corrected numbers in these samples are overestimated.

For the Run 2 analysis the $\mathrm{LLLL_L}$, $\mathrm{LLDD_L}$ and $\mathrm{DDDD_L}$ samples were utilized. While the $\mathrm{LLLL_L}$ and $\mathrm{LLDD_L}$ have similar small statistical uncertainties, the uncertainty of the $\mathrm{DDDD_L}$ sample is almost four times larger. Regarding Run 3, additional samples are considered to be incorporated. To determine whether a sample should be included, it must have higher yields than the $\mathrm{DDDD_L}$ sample. The combined statistical uncertainties of the sample combinations are reported in Table 6.2. Subsequently, the combined statistical uncertainties are compared with the combined uncertainty of the $\mathrm{LLLL_L}$, $\mathrm{LLDD_L}$ and the $\mathrm{DDDD_L}$ samples.

With reconstruction cut

If the reconstruction cut is applied for the upstream track reconstruction during the HLT2 trigger stage, the $\mathrm{LLLD_L}$ and the $\mathrm{ULLL_L}$ samples outperform the $\mathrm{DDDD_L}$ sample. Thus, these samples should be included as well. When these additional samples are integrated into future analyses an improvement in the sensitivity of 3.8% becomes achievable. By considering all samples, the potential improvement increases to 5.5%.

Table 6.2: Combined statistical uncertainty of different samples.

	samples	σ_{comb}[%]
reconstruction cut	$\mathrm{LLLL_L}$, $\mathrm{LLDD_L}$, $\mathrm{DDDD_L}$	0.65
	$\mathrm{LLLL_L}$, $\mathrm{LLDD_L}$, $\mathrm{DDDD_L}$, $\mathrm{LLLD_L}$, $\mathrm{ULLL_L}$	0.62
	all	0.61
no reconstruction cut	$\mathrm{LLLL_L}$, $\mathrm{LLDD_L}$, $\mathrm{DDDD_L}$, $\mathrm{LLLD_L}$, $\mathrm{ULLL_L}$, $\mathrm{ULDD_L}$	0.60
	all	0.60

Without reconstruction cut

If the reconstruction cut on upstream tracks is removed during the HLT2 trigger stage, the $\mathrm{ULDD_L}$ sample outperforms the $\mathrm{DDDD_L}$ sample in addition to the $\mathrm{LLLD_L}$ and $\mathrm{ULLL_L}$ samples. With the inclusion of the additional samples, an improvement of the sensitivity of the measurements by 7.0% becomes feasible.
In order to reconstruct upstream tracks, VELO tracks are extrapolated to the UT, where a search window is opened around the expected position without the influence of the stray magnetic field. Because of the magnetic field's presence, the window sizes correspond to the momentum cuts on upstream particles. An expansion of the search window is required to remove or loosen the reconstruction cut, which, in turn, leads to a slower reconstruction algorithm. Given that the current HLT2 trigger is already operating at its maximum computational capacity, it is not feasible to relax or even remove the reconstruction cut on upstream track particles. Therefore, this improvement will not be possible during Run 3. However, it may be achievable in the future.

Until now the `HLT1TwoTrackKsMVA` were omitted, leading to an underestimation in the corrected yields. To account for this, another correction as a function of the relative efficiencies of both HLT1 trigger lines has to be applied.

$$N(\frac{\epsilon'}{\epsilon}) = N_{\mathrm{corr}} + \frac{\#\, K^0_{S\,\mathrm{LL}} \text{ in sample}}{\#\, \pi_{\mathrm{L}} \text{ in sample} + 0.2} \cdot \frac{\epsilon'}{\epsilon} \cdot N_{\mathrm{corr}} \tag{6.2.3}$$

Due to the dependence on the N_{corr}, the `HLT1TwoTrackKsMVA` trigger line significantly impacts the $\mathrm{LLLL_L}$ and $\mathrm{LLDD_L}$ samples due to their high yields (Table 6.1). Whereas, in the case of $\mathrm{LLLD_L}$ and the $\mathrm{ULLL_L}$ the trigger line does not have a significant impact as their yields are a magnitude smaller compared to the $\mathrm{LLLL_L}$ and $\mathrm{LLDD_L}$ sample. Furthermore, there

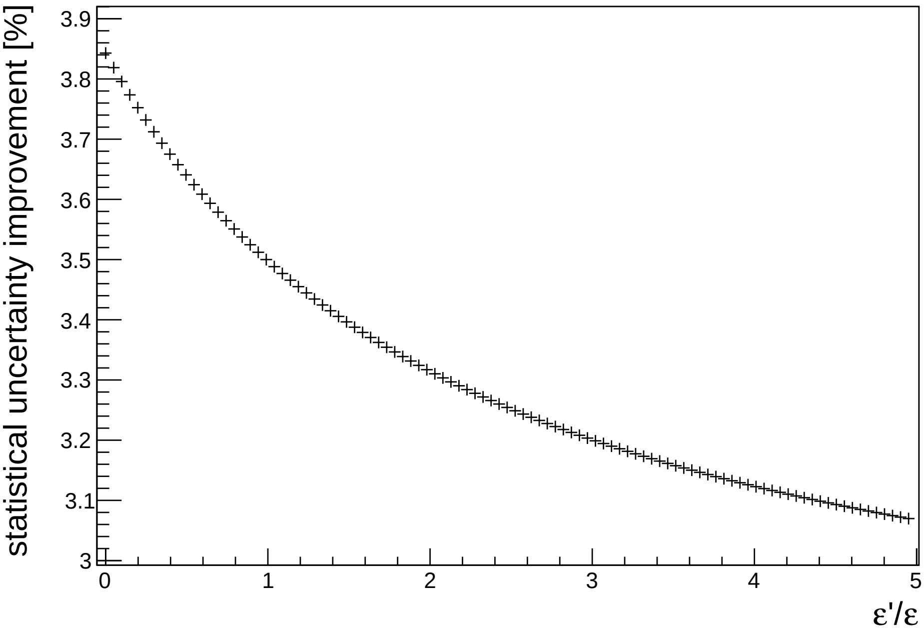

Figure 6.1: Improvement of the statistical uncertainty as a function of the relative efficiencies of the `HLT1TrackMVA` *and* `HLT1TwoTrackKsMVA` *trigger lines.*

is no change in the yields for the $\mathrm{DDDD_L}$ sample due to the absence of the $K^0_{S\,\mathrm{LL}}$ leading to no impact of the additional `HLT1TwoTrackKsMVA` trigger line. Consequently, an increase in the efficiency of the `HLT1TwoTrackKsMVA` diminishes the impact of the additional samples. Hence, the resulting graph in Figure 6.1 of the improvement of the measurement sensitivity as a function of the relative efficiencies between both HLT1 trigger lines is obtained, reaching an improvement of the sensitivity of the measurement of at least 3.1%.

Chapter 7

Exploiting upstream tracks for soft pion reconstruction

The π_{soft} used for tagging the D^0 has a mass similar to the mass difference between D^* and D^0. As a result, these π_{soft} particles have low momentum, which implies that the majority of them should be swept out of the acceptance range of the LHCb by the magnet. Hence, classifying them as upstream.
Therefore, including upstream π_{soft} samples may be of interest to increase the obtained yields per unit of luminosity. However, these samples must fulfil the exact requirements as the long track π_{soft} samples. To distinguish samples containing upstream track π_{soft} from those with long track, a subscript "U" is used in place of "L".

To obtain comparable results, the study has been performed on the same MC simulated data. The resulting yields with the default selection are summarized in Table 7.1. In the case of the LDDD_U sample no events are obtained. Resulting from these numbers, samples with upstream track π_{soft} are at least 20 times less abundant compared to long track π_{soft}.

Table 7.1: Numbers of events with default selection for long and upstream track π_{soft} samples.

π_{soft}	LLLL	LLLD	LLDD	LDDD	DDDD	ULLL	ULDD
long	1139	536	3397	561	2472	387	571
upstream	12	4	117	-	127	10	30

When considering the resolution of the K^0_S mass distributions, the same results are achieved, compared to samples with long track π_{soft}. This is because the poorer resolution of the π_{soft} does not affect the K^0_S mass distribution. However, regarding the Δm distribution, the resolution can only be determined in the LLDD_U, DDDD_U and ULDD_U samples, while for the other samples, insufficient statistics are available. The fits are performed using the same fit function as for long track π_{soft}. Additionally, an added Gaussian PDF is necessary for the LLDD_U sample. The detailed fit results with their corresponding fit parameters are reported in Appendix C, while the normalized fit functions of all samples are shown in Figure 7.1.
The FWHM values of the upstream track π_{soft} Δm distribution are reported in Table 7.2. By

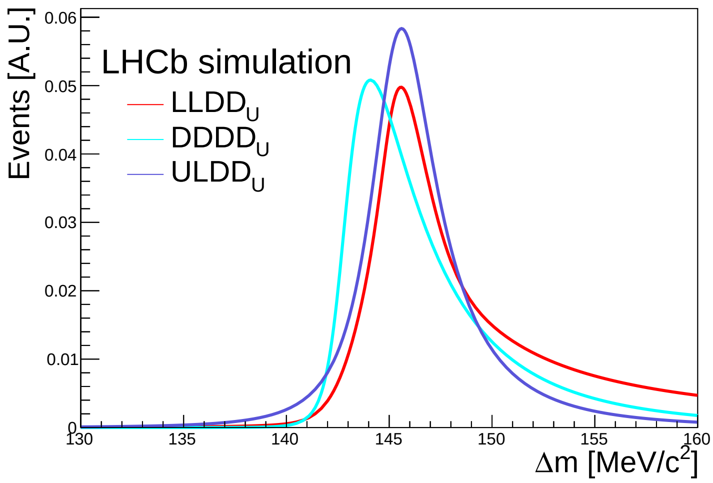

Figure 7.1: Normalized Δm distribution of all upstream π_{soft} samples where a fit is performed.

Table 7.2: FWHM values of all samples with upstream track π_{soft} where a fit is performed.

sample	FWHM [MeV/c^2]
LLDD$_L$	3.747
DDDD$_L$	3.855
ULDD$_L$	4.592

comparing to the long track π_{soft} samples (Table 4.2), an increase by at least a factor of three is observed. Consequently, when dealing with real data, it would not be feasible to accurately extract a peak and, as a result, the yields. In addition, it is expected that the resolution of the other samples, where no fit is performed, will be similar. Therefore, all samples with upstream track π_{soft} are considered unusable.

7.1 Estimate of potential gain in sensitivity

At the current stage utilizing upstream tracks for the π_{soft} reconstruction is infeasible due to their significantly worse resolution in the Δm distribution. However, the introduction of the Magnet Stations (MS) [22] for the long shutdown 4 (LS4), based on scintillating bars or fibres positioned inside the magnet, enables momenta measurement of upstream particles with similar precision as downstream tracks. Thus an improvement in the resolution is expected which might lead to their possible inclusion. Therefore, examining their potential on the statistical uncertainty of the CP asymmetry measurement becomes of interest.

Utilizing the same HLT2 trigger line, the resulting yields for samples with upstream track π_{soft} on the MC simulation on Digi format are reported in Table 7.3.
With the removal of the reconstruction cut it has become possible to reconstruct more events than when the default selection has been applied. This implies that the reconstruction cut is the primary factor of the reduction in the obtained yields, as the reconstruction cut has tighter constraints than the cut induced from the calibration channel. In Figure 7.2 the momenta

Table 7.3: Results of the HLT2 trigger line for upstream track π_{soft} without HLT1 on MC simulations.

	default selection	reconstruction cut	no reconstruction cut
$LLLL_U$	12	4	26
$LLLD_U$	4	1	4
$LLDD_U$	117	5	73
$LDDD_U$	-	1	6
$DDDD_U$	127	15	57
$ULLL_U$	10	2	13
$ULDD_U$	30	3	13

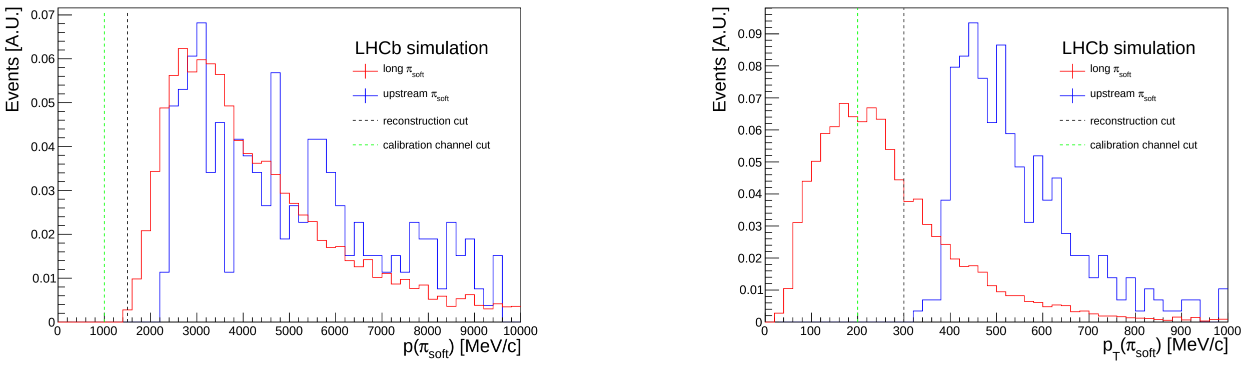

Figure 7.2: Momentum (left) and transverse momentum (right) distributions of upstream and long tracks π_{soft}. The reconstruction cut is applied only on the upstream π_{soft}, while calibration channel cuts are only visualized.

distribution for both long and upstream track π_{soft} distributions are displayed. In the case of the momentum distributions, neither the reconstruction cut nor the induced calibration channel cut has a significant effect on the event selection. However, this is not the case for the transverse momentum cuts. It is anticipated that the transverse momentum distribution of the upstream track π_{soft} should be roughly the same as the long track π_{soft} distribution, if not even lower. Thus it can be concluded that the majority of the upstream track π_{soft} events are cut off by the reconstruction cut on upstream track particles.

The results of the upstream track π_{soft} transverse momentum distribution without the reconstruction cut is shown in Figure 7.3, leading to an estimation that the reconstruction cut causes a signal loss of $\sim 60\%$.

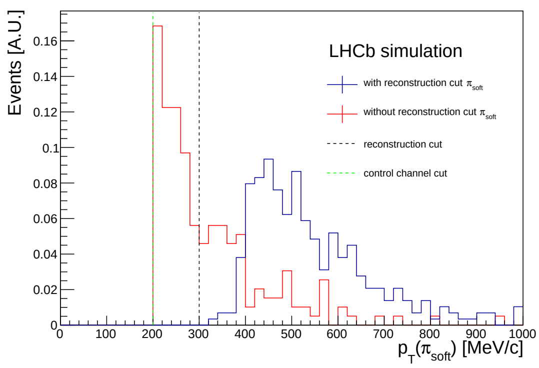

Figure 7.3: Transverse momentum distribution for upstream π_{soft} with and without loosened cut.

The impact on the sensitivity of the measurement is estimated with the same methodology derived in Section 6.1 and with the same assumptions. Soft pions are not triggered during HLT1, thus no change in the efficiency is obtained. Utilizing the yields that pass the HLT2 trigger from Table 7.3, the corrected yields with their corresponding statistical uncertainty for all upstream track π_{soft} samples are reported in Table 7.4[1].

Table 7.4: Corrected yields of each sample incorporating upstream track π_{soft} with their corresponding relative statistical uncertainty with or without the reconstruction cut.

	with reconstruction cut		without reconstruction cut	
sample	N_{corr}	$\sigma[\%]$	N_{corr}	$\sigma[\%]$
DDDD_L	718	3.7	718	3.7
LLLL_U	233	6.6	1512	2.6
LLLD_U	44	15.0	177	7.5
LLDD_U	152	8.1	2223	2.1
LDDD_U	17	24.5	100	10.0
DDDD_U	42	15.5	158	8.0
ULLL_U	89	10.6	576	4.2
ULDD_U	50	14.2	216	6.8

The results clearly show, that the inclusion of the upstream tracks π_{soft} sample does not have a significant impact on the sensitivity of the measurement if the reconstruction cut is applied during the HLT2 trigger stage. However, this changes with the removal of the reconstruction cut, resulting in the consideration of the inclusion of the LLLL_U and the LLDD_U as they then outperform the DDDD_L sample. Therefore, these two samples are added to the other long track π_{soft} samples which are considered if no reconstruction cut is applied, resulting in an expected improvement of the sensitivity in the measurement by 12.7%.

[1]It is important to note, that the statistical uncertainties of the results from the HLT2 trigger line are not taken account (Table 7.3), which also affect the shown yields.

Chapter 8

Conclusion

The $D^0 \to K_S^0 K_S^0$ decay channel is of great interest for studying CP violation and testing the Standard Model. However, the accuracy of the measurement, utilizing the LLLL_L, LLDD_L and DDDD_L samples, is limited by statistics. To address this issue, this study was performed to determine the possibility of increasing the statistics by including upstream tracks. With the removal of the hardware trigger L0 and the transition to a full software trigger, upstream tracks can be reconstructed at the first level of the trigger. Therefore, the ULLL_L, ULDD_L, LLLD_L and LDDD_L samples are considered.

Through MC simulations, the results have shown that the imprecise momentum measurement, with a precision of $\sim 15\%$ for the upstream track particles, significantly impacts the resolution of the K_S^0 mass distribution but a clear peak is still visible. However, the yields are primarily extracted from the Δm distribution, where a resolution similar to that of the LLLL_L sample is obtained. Furthermore, within the LHCb framework, a specific HLT2 trigger line is developed to select the desired events containing upstream tracks.

With the ability to select events during the HLT2 trigger stage and achieve satisfying resolution in the distributions for obtaining the yields, it becomes possible to assess the statistical uncertainties of the samples. This assessment involved utilizing the results from the HLT2 trigger, along with an efficiency estimation for correcting the HLT1 trigger effects. Hence, it is worth considering the ULLL_L and LLLD_L samples in future analyses due to an improvement of the statistical uncertainty by at least 3.1%.
Furthermore, the HLT2 trigger line incorporates the reconstruction cut on the momenta of upstream particles. Relaxing this constraint would allow the additional consideration of the inclusion of the ULDD_L sample, leading to a 7.0% improvement in the statistical uncertainty. However, this improvement is currently not possible, as relaxing the reconstruction cut would demand additional computational power, but the current HLT2 trigger is already operating at its computational limit.

Lastly, upstream track π_soft samples are considered to enhance the yields in $D^0 \to K_S^0 K_S^0$

decays. However, it has been shown that given the current experimental setup, including these samples is not feasible and not worthwhile. In order to include them in the future, the following upgrades need to be fulfilled:

1. An improvement on the precision of upstream track momenta measurement, with the Magnet Station after LS4;
2. Increased computational power, to loosen the reconstruction cut of upstream track particles.

If these requirements are fulfilled the inclusion of the $\mathrm{LLLL_U}$ and $\mathrm{LLDD_U}$ sample are considerable, resulting in an improvement of the sensitivity by 12.7%.

Further study needs to be performed on the calibration channel $D^0 \rightarrow K^+K^-$ in order to scrutinise if the momenta cuts on the π_{soft} can be loosened, which is the main contributor for the signal loss in $D^0 \rightarrow K^0_S K^0_S$ decays.

With the obtained results a merge request needs to be submitted for the developed HLT2 trigger line, in order to initiate the data collection process for the additional $\mathrm{ULLL_L}$ and $\mathrm{LLLD_L}$ samples.

Appendix A

Fit results of the K_S^0 mass distributions

The results of the K_S^0 mass distribution fit of the four K_S^0 candidates are shown in Figure A.1. For the $K^0_{S\,\mathrm{LD}}$ an added Gaussian PDF is required.

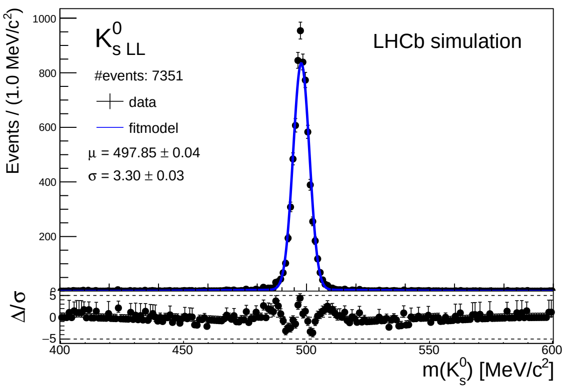

(a) $K^0_{S\,\mathrm{LL}}$.

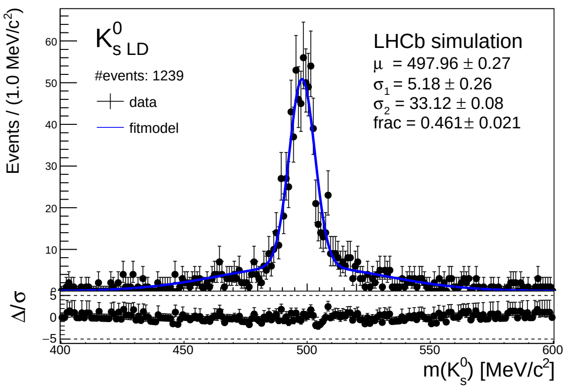

(b) $K^0_{S\,\mathrm{LD}}$.

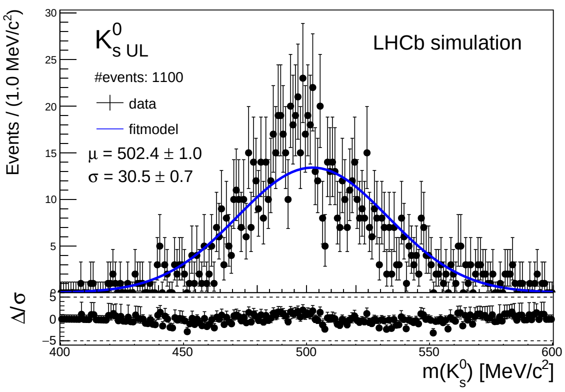

(c) $K^0_{S\,\mathrm{LL}}$.

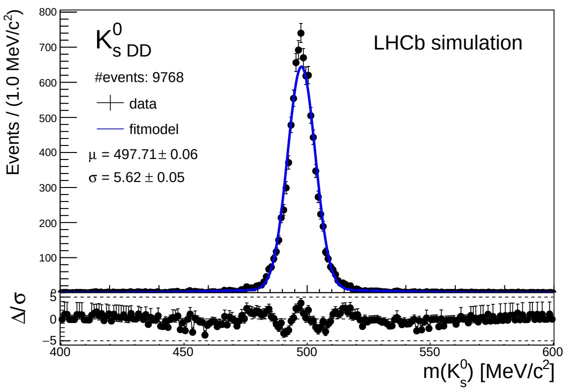

(d) $K^0_{S\,\mathrm{LD}}$.

Figure A.1: Fit of the K_S^0 mass distribution of different daughter pion track types.

Appendix B

Fit results for long track π_{soft} samples

The fit parameters resulting from the performed fit of the Δm distribution, which can be seen in Figures B.1 and B.2, are reported in Table B.1.

Table B.1: Resulting fit parameters of all Δm distributions for long track π_{soft} samples.

sample	μ [MeV/c^2]	λ [Mev/c^2]	γ	δ
LLLL$_\text{L}$	145.36 ± 0.03	0.67 ± 0.04	−0.17 ± 0.05	1.18 ± 0.05
LLLD$_\text{L}$	145.38 ± 0.04	0.42 ± 0.04	−0.11 ± 0.06	0.67 ± 0.05
LLDD$_\text{L}$	145.367 ± 0.020	0.689 ± 0.027	−0.168 ± 0.030	1.18 ± 0.03
LDDD$_\text{L}$	145.37 ± 0.04	0.55 ± 0.05	−0.17 ± 0.05	0.76 ± 0.05
DDDD$_\text{L}$	145.343 ± 0.024	0.67 ± 0.03	−0.19 ± 0.04	1.15 ± 0.04
ULLL$_\text{L}$	145.33 ± 0.05	0.58 ± 0.07	−0.20 ± 0.07	0.85 ± 0.07
ULDD$_\text{L}$	145.40 ± 0.06	0.77 ± 0.09	−0.18 ± 0.06	0.86 ± 0.08
ULUL$_\text{L}$	144.5 ± 0.5	0.92 ± 0.23	−1.2 ± 0.6	1.10 ± 0.15

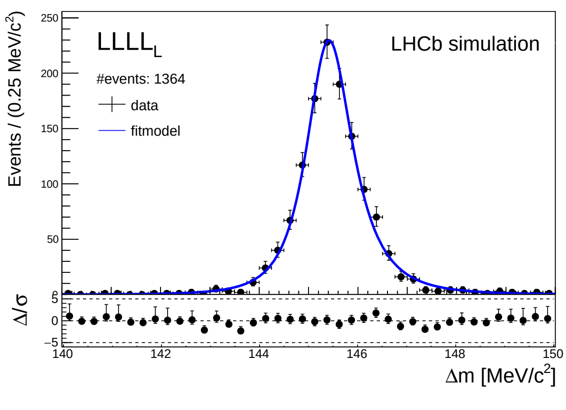

(a) LLLL$_\text{L}$ sample.

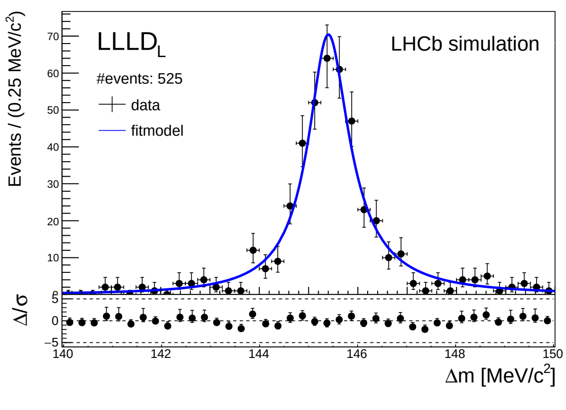

(b) LLLD$_\text{L}$ sample.

Figure B.1: Fit of the Δm distribution for long track π_{soft} samples.

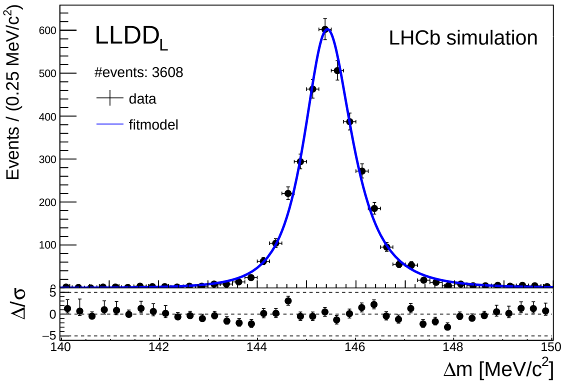

(a) LLDD$_L$ sample.

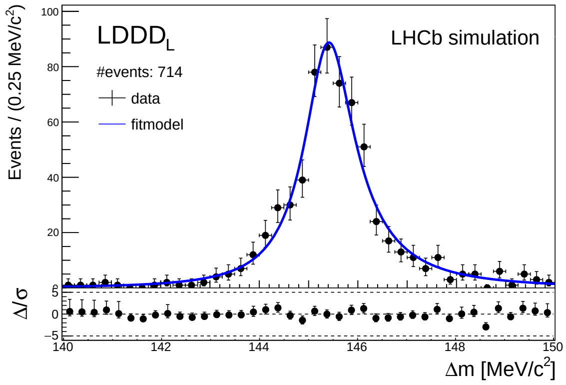

(b) LDDD$_L$ sample.

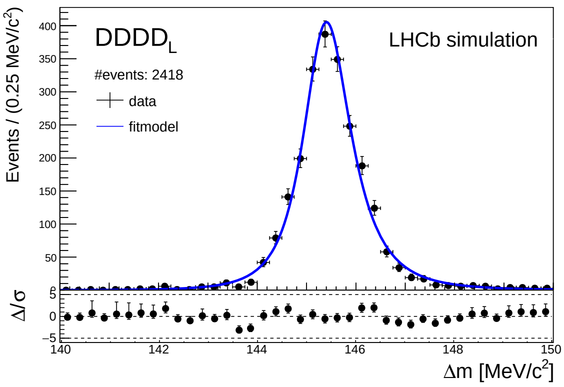

(c) DDDD$_L$ sample.

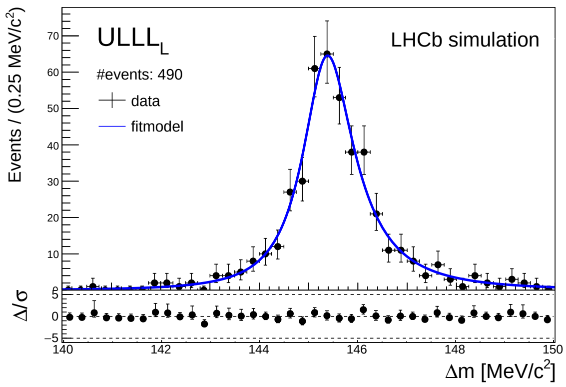

(d) ULLL$_L$ sample.

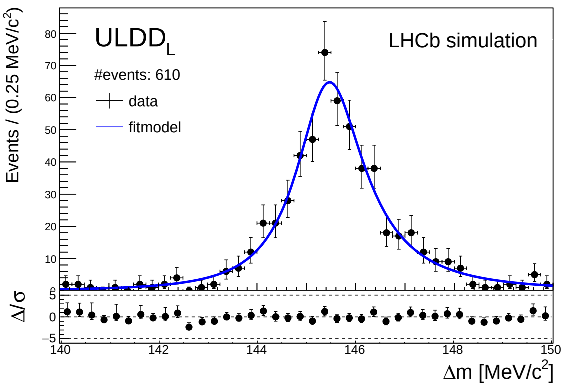

(e) ULDD$_L$ sample.

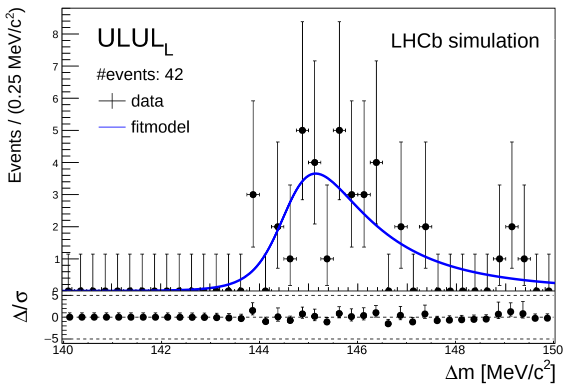

(f) ULUL$_L$ sample.

Figure B.2: Fit of the Δm distribution for long track π_{soft} samples.

Appendix C

Fit results for upstream track π_{soft} samples

The fit parameter resulting from the performed fit of the Δm distribution, which can be seen in Figures C.1 and C.2, are reported in Tables C.1 and C.2. In the case of the LLDD_U sample an added Gaussian PDF is required.

Table C.1: Resulting fit parameters of all Δm distributions for upstream track π_{soft} samples.

sample	μ [MeV/c^2]	λ [Mev/c^2]	γ	δ
DDDD_U	142.6 ± 0.6	1.36 ± 0.13	-1.7 ± 0.4	1.05 ± 0.17
ULDD_L	145.24 ± 0.08	1.8 ± 0.4	-0.4 ± 0.4	0.90 ± 0.19

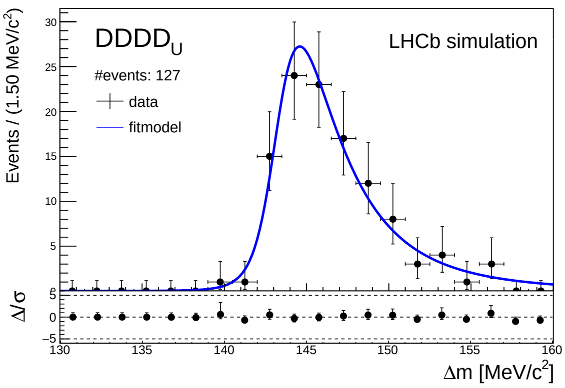

(a) LLLL_U sample.

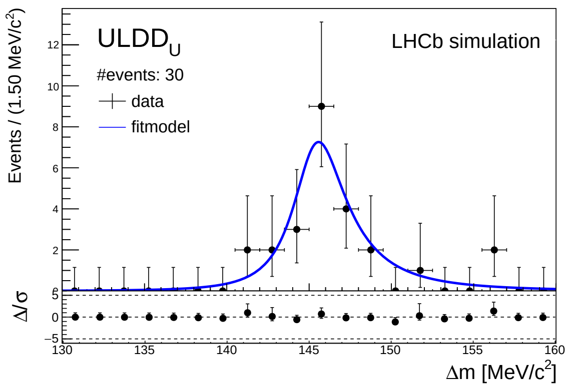

(b) LLLD_U sample.

Figure C.1: Fit of the Δm distribution for upstream track π_{soft} samples.

Table C.2: Resulting fit parameters for the LLDD_U sample.

	LLDD_U
μ [MeV/c^2]	145.0 ± 0.3
σ [MeV/c^2]	1.5 ± 0.4
λ [MeV/c^2]	1.09 ± 0.12
γ	-1.4 ± 0.7
δ	0.55 ± 0.15
frac	0.22 ± 0.27

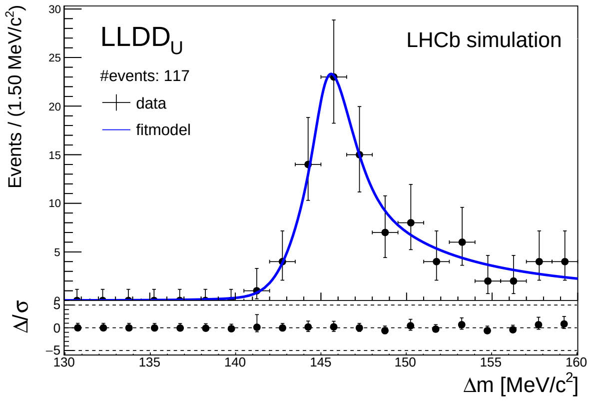

Figure C.2: Fit of the Δm distribution in the LLDD$_{\mathrm{U}}$ sample.

Bibliography

[1] Ulrich Nierste and Stefan Schacht. "*CP* violation in $D^0 \to K_S K_S$". In: *Phys. Rev. D* 92 (5 Sept. 2015), p. 054036. DOI: 10.1103/PhysRevD.92.054036. arXiv: 1508.00074 [hep-ex].

[2] Giulia Tuci. "Searching for confirmation of charm CP violation in K_S^0 final states at LHCb". PhD thesis. CERN-THESIS-2020-325, University of Pisa, Pisa, 2021.

[3] M Thomson. *Modern Particle Physics*. Cambridge: Cambridge University Press, 2013.

[4] Wikimedia Commons. Standard Model of Elementary Particles. URL: https://en.wikipedia.org/wiki/File:Standard_Model_of_Elementary_Particles.svg.

[5] Particle Data Group et al. "Review of Particle Physics". In: *Progress of Theoretical and Experimental Physics* 2022.8 (Aug. 2022), p. 083C01. ISSN: 2050-3911. DOI: 10.1093/ptep/ptac097.

[6] E Kou et al. "The Belle II Physics Book". In: *Progress of Theoretical and Experimental Physics* 2019.12 (Dec. 2019), p. 123C01. ISSN: 2050-3911. DOI: 10.1093/ptep/ptz106.

[7] N. Dash et al. "Search for *CP* Violation and Measurement of the Branching Fraction in the Decay $D^0 \to K_S^0 K_S^0$". In: *Phys. Rev. Lett.* 119 (17 Oct. 2017), p. 171801. DOI: 10.1103/PhysRevLett.119.171801.

[8] Lyndon Evans and Philip Bryant. "LHC Machine". In: *Journal of Instrumentation* 3.08 (Aug. 2008), S08001. DOI: 10.1088/1748-0221/3/08/S08001.

[9] LHCb collaboration et al. *The LHCb upgrade I*. 2023. arXiv: 2305.10515 [hep-ex].

[10] LHCb collaboration et al. "LHCb VELO Upgrade Technical Design Report". In: *CERN-LHCC-2001-011, LHCb-TDR-013* (2013).

[11] LHCb collaboration et al. "LHCb Tracker Upgrade Technical Design Report". In: *CERN-LHCC-2014-001, LHCB-TDR-015* (Feb. 2014).

[12] LHCb RICH Collaboration et al. "Performance of the LHCb RICH detector at the LHC". In: *Eur. Phys. J. C 73, 2431* (Mar. 2013). DOI: 10.1140/epjc/s10052-013-2431-9.

[13] C. Abellán Beteta et al. *Calibration and performance of the LHCb calorimeters in Run 1 and 2 at the LHC*. 2020. arXiv: 2008.11556 [physics.ins-det].

[14] LHCb collaboration et al. *RTA and DPA dataflow diagrams for Run 1, Run 2, and the upgraded LHCb detector*. In report number LHCb-FIGURE-2020-016. 2020.

[15] M Clemencic et al. "The LHCb Simulation Application, Gauss: Design, Evolution and Experience". In: *Journal of Physics: Conference Series* 331.3 (Dec. 2011), p. 032023. doi: 10.1088/1742-6596/331/3/032023.

[16] R. Antunes Nobrega et al. "LHCb Computing Technical Design Report". In: *Technical Design Report LHCb* (2005).

[17] Torbjörn Sjöstrand et al. "An introduction to PYTHIA 8.2". In: *Computer Physics Communications* 191 (2015), pp. 159–177. issn: 0010-4655. doi: https://doi.org/10.1016/j.cpc.2015.01.024.

[18] David J. Lange. "The EvtGen particle decay simulation package". In: *Nuclear Instruments and Methods in Physics Research Section A: Accelerators, Spectrometers, Detectors and Associated Equipment* 462.1 (2001). BEAUTY2000, Proceedings of the 7th Int. Conf. on B-Physics at Hadron Machines, pp. 152–155. issn: 0168-9002. doi: https://doi.org/10.1016/S0168-9002(01)00089-4.

[19] S. Agostinelli et al. "Geant4—a simulation toolkit". In: *Nuclear Instruments and Methods in Physics Research Section A: Accelerators, Spectrometers, Detectors and Associated Equipment* 506.3 (2003), pp. 250–303. issn: 0168-9002. doi: https://doi.org/10.1016/S0168-9002(03)01368-8.

[20] N. L. JOHNSON. "SYSTEMS OF FREQUENCY CURVES GENERATED BY METHODS OF TRANSLATION". In: *Biometrika* 36.1-2 (June 1949), pp. 149–176. issn: 0006-3444. doi: 10.1093/biomet/36.1-2.149.

[21] A. Hoecker et al. *TMVA - Toolkit for Multivariate Data Analysis*. 2007. arXiv: physics/0703039 [physics.data-an].

[22] Roel Aaij et al. *Expression of Interest for a Phase-II LHCb Upgrade: Opportunities in flavour physics, and beyond, in the HL-LHC era*. Tech. rep. Geneva: CERN, 2017.

Acknowledgments

First of all, I would like to express my gratitude to Prof. Stephanie Hansmann-Menzemer for providing me with the opportunity to work in your LHCb group.
I would like to thank Dr. Giulia Tuci for the interesting topic of my thesis, as well as the support throughout the whole thesis.
Special thanks to my office mates for providing such a friendly and peaceful working environment as well as for the interesting topics that we discussed throughout our time here. Also thanks to the "pseudo-bachelor" for offering his 木剣 during times of emergencies. I am also thankful to the LHCb for welcoming me into the group.
I would like to express my deepest gratitude to my family and my friends without them I would not have come this far.